Electron bunches from an ultra-cold plasma source

Smakman, E.P.

Award date:
2010

Eindhoven University of Technology
Department of Applied Physics
Coherence and Quantum Technology (CQT)
CQT 2010-03

Electron Bunches from an Ultra-Cold Plasma Source

E.P. Smakman

April 8, 2010

Supervisors:
O.J. Luiten
E.J.D. Vredenbregt

Abstract

Ultrafast electron diffraction (UED) is a method to observe physical, chemical and biological structures on a nm-scale and a sub-ps timescale, enabling the study of reactions and phase transitions. With enough electron bunch charge, single-shot UED can be performed. A low bunch emittance allows the study of large biological crystals, for example proteins.

An ultra-cold plasma (UCP) is a new type of source for electron bunches with low transverse emittance, because of the very low electron temperature. The UCP is created from a laser-cooled gas of Rb atoms. A laser ionizes a part of this gas, and the created electrons can be accelerated by means of an applied electric field. Experiments have been performed to measure the transverse temperature of the electron bunches created in an UCP setup. The transverse sizes of the bunches have been measured after transport through a beam line. Analysis of these sizes resulted in an electron temperature at the source. The temperature is dependent on the excess energy, which is the extra energy above the ionization threshold an electron gains in the ionization process. The excess energy is determined by the ionization laser wavelength and the applied electric field strength.

A series of photoionization experiments in a DC electric field shows that the transverse temperature of the electrons can be set to a range of $T =$ 10 - 500 K by varying the excess energy. The transverse temperature is lower compared to that calculated with a linear model of an identical bunch momentum distribution in all three directions. Two dynamical models for the temperature take into account the ionic Coulomb potential and the linear Stark potential from the applied electric field. These models show similar non-linear behaviour as the data, but do not completely agree quantitatively. A temperature as low as $T = 10.7 \pm 0.8$ K has been measured, which is in the temperature range that is needed for single-shot UED of proteins. However, more charge per bunch, shorter pulse lengths and higher electron energies are needed before this type of experiment can actually be performed.

In another series of experiments, Rydberg energy levels in the Rb atom have been used together with a pulsed electric field to field-ionize electrons and potentially create bunches with a very small temporal length. An indicative temperature of $T = 50$ K is calculated using multiple Rydberg states, showing that low temperature is also possible for this type of ionization.

Contents

Chapter 1

Introduction

Ultrafast electron diffraction (UED) is a method to study structures on a nm-scale and very small timescales, with many applications in physics, chemistry and biology. It uses electron bunches to generate diffraction patterns from a sample, which can be used to analyze the composition of the material. Recent studies have shown the possibility of imaging structural changes in complex molecular systems on a sub-ps timescale [1]. Here, UED enables the study of transient structures of a chemical reaction, which gives more understanding of the underlying intermediate processes.

Another application of UED is the recording of a phase transition, for example the melting of Aluminum presented in ref. [2] and illustrated in Figure 1.1. With intervals of 500 fs, pump-probe experiments were performed on a sample. A 120 fs laser pulse induces the solid-liquid phase transition in the metal, while a synchronized electron bunch records the diffraction pattern at the chosen delay time. This is then repeated multiple times, allowing the sample to relax back to its original solid state in between. A combination of 150 diffraction patterns gave enough information to image a single time step. The complete phase transition of 3.5 ps was recorded and provided an atomic-level description of the reaction.

Single-shot UED is a logical next step as an imaging method, in which one electron bunch records a complete diffraction pattern containing enough information for analysis of a single time step. It enables the making of a 'molecular movie' [3]. This opens the possibility to study biological and chemical reactions in samples that are destroyed in the measurement, or do not relax back to their original state after the reaction. It requires high-charge electron bunches to extract all information in a single shot. With single-shot UED, a lot of new ultrafast processes could be studied without using a huge amount of samples.

The quality of an electron beam can be expressed in terms of emittance, which is the volume an electron bunch occupies in phase space. This quantity is further explained in Section 1.1. An example of a typical electron source

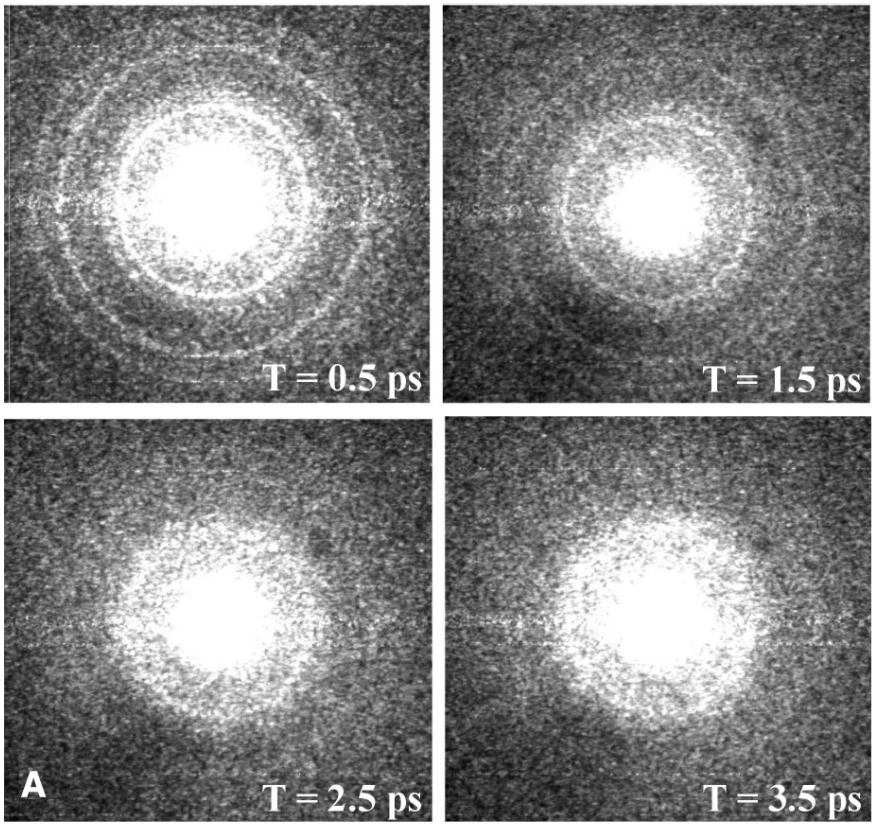

Figure 1.1 UED study of the solid-liquid phase transition in Al. Intensity profiles of 150 diffracted electron pulses were taken at different pump-probe delay intervals on a ps timescale. The first pattern has rings corresponding to a fcc lattice structure (solid), while the last pattern shows only one broad ring (liquid). From [2].

for UED is given in Section 1.2. In this type of source, a fs laser pulse frees electrons from a cathode surface. However, it is shown that this source is not suitable for single-shot UED when looking at protein crystals, because of the high electron temperature. Proteins typically have a substantially larger lattice spacing than atomic lattices, which makes it harder to extract a diffraction pattern.

A new table-top electron source employing an ultra-cold plasma (UCP) is discussed in Section 1.3. A low transverse emittance can be obtained by ionizing and extracting very cold electrons from a magneto-optical trap (MOT). This is a new type of source, which has not been used much outside of fundamental research. It has the potential to become a source for single-shot UED, also for protein crystals. This thesis addresses the temperature of electron bunches created in the UCP setup. The precise goals of this thesis are outlined in Section 1.4.

1.1 Emittance

The quality of an electron beam can be expressed in terms of emittance, or the volume it occupies in phase space. Phase space combines position coordinates x, y and z with momentum coordinates p_x, p_y and p_z for all electrons in a bunch at a certain time. The smaller the volume the bunch occupies in this 6D phase space, the higher the quality of the beam. Better quality in this context means that for a given angular spread, the bunch can be focussed to a smaller spot.

1.1.1 Position and Momentum

For one dimension in position space or two dimensions in phase space, a perfect non-interacting beam with zero emittance is shown in Figure 1.2 [4]. This is a particle beam with so-called laminar flow: none of the particle trajectories intersect each other except at the focal point. Figure (a) shows the particle trajectories of an electron bunch going through a lens and being focussed at a point. Figure (b) shows the phase space plot at three different times: before the lens (1), just after the lens (2) and at the focal point (3).

At point (1), electrons all move in one direction and therefore occupy only an infinitely thin line in position space. The lens gives the particles a momentum distribution. This distribution is position dependent: upper electrons get a momentum downwards and vice versa. This can be seen in the emittance figure at point (2) as a rotation and a stretching of the line with respect to point (1). The projection on the x-axis is still the same, because the bunch has not become smaller at this point. Finally, at point (3), the bunch has been focussed to a single point and the momentum distribution is the same as in point (2).

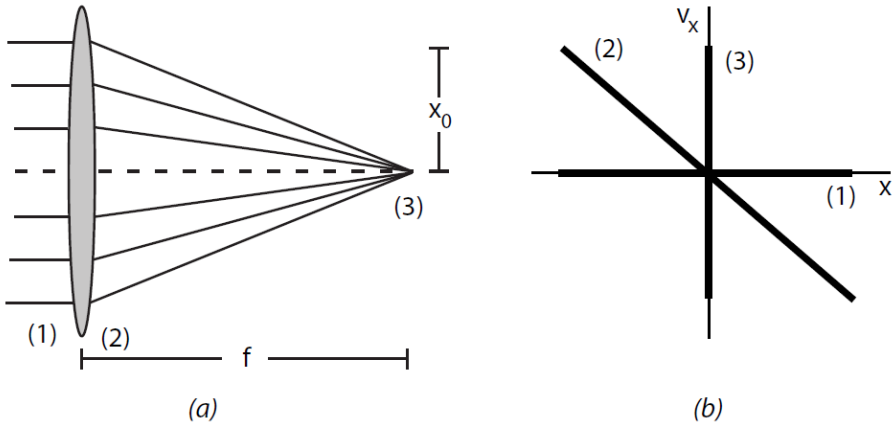

Figure 1.2 Particle trajectories (a) and emittance in phase space (b) for a laminar electron bunch with radius x_0 focussed by lens with focal length f. The positions in (a) correspond to the plots in (b). Image from ref. [4].

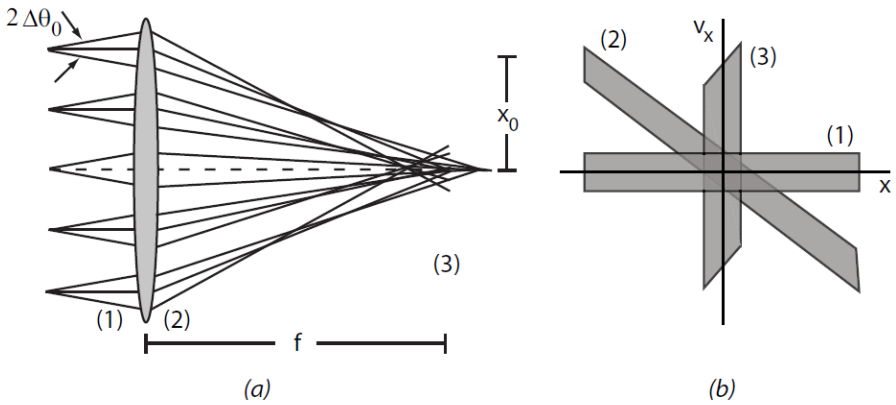

Figure 1.3 Particle trajectories (a) and emittance in phase space (b) for a non-laminar electron bunch with radius x_0 and divergence $\Delta\theta_0$ focussed by lens with focal length f. The positions in (a) correspond to the plots in (b). Image from ref. [4].

Obviously, this example does not represent a real electron bunch. The initial momentum spread of the bunch is not zero. What happens in this case is illustrated in Figure 1.3 [4]. An electron bunch with initial momentum spread or divergence going through the same (ideal) lens as before now occupies a finite surface in phase space. As in the previous example, the lens rotates and stretches this surface by giving the electrons additional momentum. At point (2), the shape has changed of the occupied area in phase space. This is true because the position spread of the bunch did not change, so the length in the x-direction is the same. The surface still occupies the same area, or in other words, the emittance is conserved. This again holds for point (3), where the electron bunch has lost position spread and gained momentum spread, but still occupies the same finite volume in phase-space. This conservation of phase-space is known as Liouville's theorem. This theory is valid if the amount of particles in the bunch is large and there are no significant sources of emittance growth.

There are interactions between electrons in the form of space charge forces and collisions between particles, which both increase the emittance of the bunch. Lenses are not ideal and have aberrations which further increase the emittance. Emittance growth leads to distortion in the electron bunches that cannot be corrected by linear particle lenses. If a high quality electron beam is the goal, emittance growth should be avoided as much as possible in the trajectory that the bunches follow after creation. Starting out with a low emittance beam is then also of importance, which is the goal of this project.

1.1.2 Emittance and Temperature

The normalized root-mean-square (rms) emittance ϵ_x of an electron bunch in the x-direction is [5]:

$$\epsilon_x = \frac{1}{m_e c}\sqrt{< x >^2 < p_x >^2 - < x p_x >^2}, \tag{1.1}$$

where m_e is the electron mass, c the speed of light, x the position of an electron with respect to the average bunch position and p_x the momentum with respect to the average momentum. $< .. >$ indicates the average of the quantity over the ensemble of electrons in the bunch. The emittance is normalized to the acceleration energy of an electron bunch.

If there is no correlation between position and momentum, for example at the source or in a beam waist, $< x p_x >= 0$ and Eq. 1.1 reduces to:

$$\epsilon_x = \frac{1}{m_e c}\sigma_{x_i}\sigma_{p_{xi}}, \tag{1.2}$$

where σ_{x_i} is the rms source spot size and $\sigma_{p_{xi}}$ the rms source momentum, both in the x-direction (i from initial).

The kinetic energy related to the rms initial momentum $\sigma_{p_{xi}}$ can be expressed as a thermal motion of electrons [6]:

$$\frac{1}{2}\frac{\sigma_{p_{xi}}^2}{m_e} = \frac{1}{2}k_B T, \tag{1.3}$$

where k_B is Boltzmann's constant and T is the electron temperature of the source. Note that the factor 1/2 on the right side applies to motion in a single direction. Eqs. 1.2 and 1.3 lead to a new expression for the emittance:

$$\epsilon_{x_i} = \sigma_{x_i}\sqrt{\frac{k_B T}{m_e c^2}}. \tag{1.4}$$

The equation shows the emittance can be reduced by lowering the temperature.

1.2 Electron Source for UED

For single-shot UED experiments, there are optimal quantities for several electron bunch properties [6, 7]. The optimal energy range for electrons is between $U = 100 - 300$ keV. For energies lower than that, the transmission through the sample is worse, while at higher energies the interaction with the sample becomes weaker (e.g. there are reduced cross-sections for elastic scattering). Bunch charges should be typically $Q = 100$ fC, because then single-shot UED measurements contain enough signal for analysis. Rms temporal bunch lengths of $\sigma_t \leq 100$ fs enable the study of the very fast processes and rms energy spreads of $\sigma_U \leq 1$ keV ensure a sharp diffraction pattern.

The relevant quantity that then remains is the transverse coherence length $L_\perp$. To perform electron diffraction measurements, $L_\perp > a$, where a is the lattice spacing of the sample of interest. The diffraction patterns are then clearly visible. $L_\perp$ can be written as [7]:

$$L_\perp = \frac{\hbar}{m_e c}\frac{\sigma_{x_f}}{\epsilon_{x_i}}, \tag{1.5}$$

where $\hbar$ is the reduced Planck constant and σ_{x_f} is the rms spot size on the sample (f from final). Combining Eqs. 1.4 and 1.5 then gives for a thermal source:

$$L_\perp = \frac{\hbar}{\sqrt{m_e k_B T}}\frac{\sigma_{x_f}}{\sigma_{x_i}}. \tag{1.6}$$

Protein crystals of interest are for example Myoglobin with $a = 4$ nm and Hemoglobin with $a = 6$ nm [8]. These protein crystals maximally have

sizes of $\sigma_{x_f} = 100$ μm. Minimal obtainable initial sizes of electron bunches are around $\sigma_{x_i} = 25$ μm. Smaller initial sizes are difficult to create with lasers. Also, electron bunches then suffer from more space charge effects that lead to emittance growth.

An example of a compact, state-of-the-art electron source suitable for UED is the DC photogun currently being developed in the CQT group [7]. Electron bunches are created by a high intensity femtosecond laser pulse hitting a metal cathode surface. The created bunches are accelerated with a DC electric field to $U = 100$ keV. The bunches are then compressed longitudinally by a radio frequency (rf) cavity. A rf cavity produces an alternating electric field in the direction of acceleration. If the phase of the field is time-synchronized correctly with the pulse of the ionization laser, the electrons at the front of the bunch are slightly decelerated, while the ones at the back are slightly accelerated. This effectively compresses the bunch. A sample can be put at the point where the bunch is the shortest, enabling bunch lengths of around $\sigma_t = 100$ fs. The electron temperature for photoguns is typically $T = 5000$ K [6]. From Eq. 1.6, the coherence length for the rf photogun then is $L_\perp = 2$ nm, which is not good enough to perform single-shot UED on protein crystals.

1.3 Electron Source for Single-Shot UED

For single-shot UED of a typical protein, the DC photogun mentioned in Section 1.2 does not have a high enough coherence length. As can be seen from Eq. 1.6, a solution to this problem is using electron bunches with a lower temperature. In the CQT group, a new type of electron source is being developed, employing an ultra-cold plasma (UCP) in an accelerator structure [4, 9]. The UCP source can in principle supply electron bunches with temperatures down to at least $T = 10$ K for electron bunch pulse lengths of $\sigma_t = 1$ ps [6]. Following the same calculation as for the rf photogun, a coherence length of $L_\perp = 38$ nm can then be obtained. These electron bunches would be suitable for the single-shot UED study of the proteins mentioned in Section 1.2 and many other crystallic structures.

1.3.1 Ultra-Cold Plasma

An ultra-cold plasma is created from a laser-cooled gas cloud of neutral atoms. The plasma is induced by photoionization of the atoms just above threshold using a pulsed laser [10]. Electron temperatures of these type of plasmas can in principle go below $T = 1$ K [11]. Electron bunches are extracted from the plasma with a DC or pulsed electric field.

In the setup of the CQT group, a laser cooled atomic cloud of Rb is used. It can have densities up to $n_a = 10^{18}$ m^{-3}, with a rms size of $\sigma_a = 1$ mm. Up to $Q = 1$ nC electron bunches can be extracted from such a cloud in theory.

However, in measurements discussed in this thesis to determine the electron temperature of the source, electron bunches with typically $Q = 1 - 100$ fC were used.

The low temperature of the laser cooled bunches is limited by a process called disorder-induced heating. This occurs for densities in the UCP at which the Coulomb interaction becomes important [6]. The randomly distributed electrons then will heat up until the kinetic energy $3/2k_BT$ is in equilibrium with the potential Coulomb energy $e^2/(4\pi\epsilon_0 r_a)$, with r_a the average distance between two atoms. With the single-shot UED conditions for electron bunches mentioned in Section 1.2, this results in $T_h = 2$ K as a minimum temperature. This temperature is reached within a timescale in the order of the inverse plasma frequency $\omega_p^{-1} = \sqrt{m_e\epsilon_0/(n_e e^2)} = 0.4$ ns, where n_e is the electron density [6]. For acceleration energies of $U = 100$ keV, this translates into a travelling distance of 0.1 m, which is clearly relevant for the current setup beam line with a length of $d_{tot} = 1.53$ m.

There is an additional process that limits low electron temperature, which is related to the ionization time. If the ionization laser pulse has a rms pulse length of σ_t, from the Heisenberg uncertainty principle it follows that the minimum rms bandwidth energy of the laser is $\sigma_i = \hbar/(2\sigma_t)$. This results in a minimum temperature by equating σ_i to the kinetic energy of the electrons of $3/2k_BT$. For $\sigma_t = 1$ ps, this gives $T_i = 3$ K [6].

These temperature limits start to become important if single-shot UED is performed, which is not yet a possibility in the current setup. The electron temperature that was measured in the photoionization experiments described in this thesis were done with an ionization laser pulse length of $\sigma_t = 2.5$ ns [12] and energies of typically $U = 1$ keV. These numbers result in a disorder-induced heating temperature of $T_h = 0.2$ K and a bandwidth temperature of $T_i = 2$ mK. This means these effects should not play a role in the experiments above $T = 1$ K.

1.3.2 Previous Results

Experiments have been done previously to study the electron temperature by Taban [4]. One important parameter in the presented work is the wavelength of the ionization laser, which determines the excess energy the electrons gain from the ionization process that occurs just above threshold. It became clear that the electron temperature is tunable by changing the wavelength of the ionization laser. It was possible to reach a temperature of around $T = 10$ K in the measurements.

In principle, lower temperatures should be possible, but measurements were limited by the temperature resolution of the setup. Another problem was that only averaged temperatures could be determined, because the temperature could only be calculated from a dataset with variable electron energies. The energy is dependent on the accelerator electric field strength,

and the field strength in turn causes a Stark energy shift in the ionization threshold. A change in ionization threshold means a different electron temperature. It means that the electron energy and temperature are dependent on each other, and therefore only averaged temperatures could be calculated.

1.4 This Thesis

In this thesis the focus lies on measuring and modelling of the electron temperature in the UCP source. The source temperature is investigated in a new beam line that is longer and therefore has a better temperature resolution than before. Also, a magnetic solenoid lens has been designed and implemented in the setup. The focal length of the lens can be used as an independent scan parameter for a measurement of a single temperature at a single electron energy. A measurement of the temperature consists of varying the focal length of lens and measuring the spot size of the electron bunches on a detector. From this, the temperature can be determined using an optical model for the electron trajectories in the beam line.

The main goal in this thesis is investigating the electron transverse temperature behaviour with respect to the relevant parameters that determine the excess energy of the electrons. Therefore, the dependence of temperature on ionization laser wavelength and electric field strength has been measured. This was done by photoionization of Rb atoms in a DC electric field.

Another ionization scheme of Rb was also explored, using Rydberg atoms in a pulsed electric field. Field-ionization can in principle create very short temporal bunch lengths that might be suitable for single-shot UED. It is unclear what transverse temperature of electrons can be reached with this method. Measurements of the temperature were performed in the old setup, so that only an averaged temperature over an energy range could be calculated.

In Chapter 2, the UCP source is described in more detail. Chapter 3 treats the model and analysis which are used to derive an electron source temperature from the measurements. In Chapter 4 the experimental results are presented. Chapter 5 contains conclusions and recommendations.

Chapter 2

Ultra-Cold Plasma Electron Source

In Chapter 1, a new type of source for pulsed electron beams is introduced, the ultra-cold plasma (UCP). Electron bunches created in an UCP can in principle have a low transversal emittance, which makes them ideal candidates for single-shot UED experiments.

In Chapter 4, measurements of the source temperature are presented that are obtained by measuring electron bunch sizes on a detector. The relation between bunch size and source temperature is treated in Chapter 3. In this chapter, the UCP source is described in detail. In Section 2.1, laser cooling and trapping is explained. The ionization and acceleration process is the subject of Section 2.2. The beam line and detector are considered in Section 2.3. A short description of the software used to control the experiments is given in Section 2.4.

2.1 Magneto-Optical Trap

In the UCP setup, Rubidium atoms are cooled and trapped with a magneto-optical trap (MOT) [13]. The operating principle of a MOT is based on laser cooling of a gas combined with a magnetic quadrupole for trapping.

2.1.1 Cooling

The concept of Doppler laser cooling is illustrated in Figure 2.1 [9]. Consider an atom with momentum $\mathbf{p} = m\mathbf{v}$ travelling in one direction, where m is the mass and $\mathbf{v}$ the velocity. In the opposite direction, a laser is directed, with wavevector $\mathbf{k} = 2\pi\hat{k}/\lambda$, where λ is the wavelength of the laser and $\hat{k}$ is the unit vector pointing in the same direction as the laser. The atom can absorb a photon from the laser beam, which excites the atom from the ground state $\mid g >$ to the excited state $\mid e >$. The photon carries a momentum $\hbar\mathbf{k}$, which

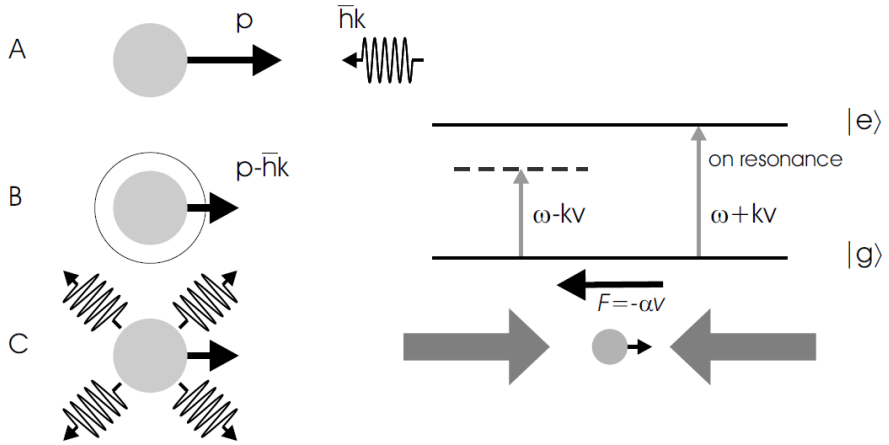

Figure 2.1 Explanation of the Doppler laser cooling effect. An atom is hit by a photon moving in the opposite direction (left, A). The atom is excited from the ground state $\mid g >$ to the excited state $\mid e >$ and its momentum is reduced (B). When the atom decays back to $\mid g >$, it emits the photon in a random direction (C). Two counter-propagating laser beams have a different detuning from the transition due to the Doppler effect (right, top). The net result is a velocity dependent force that slows down the atom with damping coefficient α (bottom). From [9].

gives the atom a recoil in the opposite direction of its motion. The atom decays back to its ground state after a typical time $\tau = 1/\Gamma$, with Γ the natural linewidth of the transition. The atom then spontaneously emits the photon in a random direction. The total momentum the atom gains from many photons adds up for absorption, but it averages out to zero for emission. This means the scattering of many photons results in a net force that slows down the atom. This process is called laser cooling.

The force a laser beam exerts on an atom is [13]:

$$\mathbf{F}_\delta = \hbar\mathbf{k}\frac{\Gamma}{2}\frac{s}{1+s+(2\delta/\Gamma)^2}. \tag{2.1}$$

Here, $s = I/I_0$ is the saturation parameter with I the intensity of the laser and I_0 the so-called saturation intensity, a property of the atom. The detuning $\delta = \omega - \omega_0 - \mathbf{k}\cdot\mathbf{v}$ is the difference of the laser frequency ω compared from the atomic resonance frequency ω_0. The extra term $\mathbf{k}\cdot\mathbf{v}$ represents the Doppler shift of an atom with respect to the laser beam direction.

Now consider a cloud of atoms that is cooled by two counter-propagating laser beams that are red-detuned ($\omega - \omega_0 < 0$). The beams exert forces on the atoms from both sides in opposite directions. The velocity of the atom introduces an imbalance in the forces of the two laser beams. An atom that moves in the forward direction experiences a larger force from the beam propagating in the backward direction, because the Doppler shift decreases

the detuning, see Figure 2.1. For the beam propagating in the same direction as the atom, the Doppler shift increases the detuning and thus reduces the force. The scattering of many photons gives a net force that slows down the atom. The combination of the laser beams narrows the velocity distribution of the atom cloud, or in other words: it cools down the atoms. Laser cooling can be applied in all three dimensions using six laser beams. For small Doppler shifts the force on an atom can be expressed as a damping force with damping coefficient α [13]:

$$\mathbf{F_D} = -\alpha \mathbf{v}. \tag{2.2}$$

Spontaneous emission limits the cooling of atoms, because photons are emitted by the atom in a random direction. The atoms will therefore never completely stop moving, resulting in a temperature limit. This temperature is the Doppler cooling limit [13]:

$$T_D = \frac{\hbar\Gamma}{2k_B}. \tag{2.3}$$

2.1.2 Trapping

The force considered so far reduces the velocity of the atoms, but does not prevent them from moving out of the region where the laser beams propagate and where the cooling occurs. To solve this problem, a position dependent force must be added to create a trap. This can be done by adding a magnetic field gradient to the system and choosing the correct polarization for the laser beams. The result is a MOT. The concept of trapping is illustrated in Figure 2.2 [9].

In the MOT, six orthogonal red-detuned, counter-propagating, circular-polarized laser beams intersect. The point of intersection is the center of a magnetic quadrupole field. The field is created by two parallel coils at opposite ends, at a distance from each other equal to their diameter, with current flowing in the opposite direction (which is called the anti-Helmholtz configuration). The quadrupole field creates a linear magnetic field gradient which induces a linear Zeeman splitting of degenerate atomic transitions with different magnetic quantum numbers M_J.

The explanation for trapping is now given for the ground state $\mid g >$ of the atom with angular momentum quantum number $J = 0$ and excited state $\mid e >$ with $J = 1$. The Zeeman shift splits the degenerate levels $M_J = 0, \pm 1$ of $\mid e >$ outside the center of the MOT. The Zeeman shift that lowers the transition energy level reduces the detuning. Analogous to laser cooling, photons exciting the atom to this lowered energy level exert a larger force on the atom. However, now this force is position dependent instead of velocity dependent. Farther away from the MOT, the Zeeman shift is larger, resulting in a larger force.

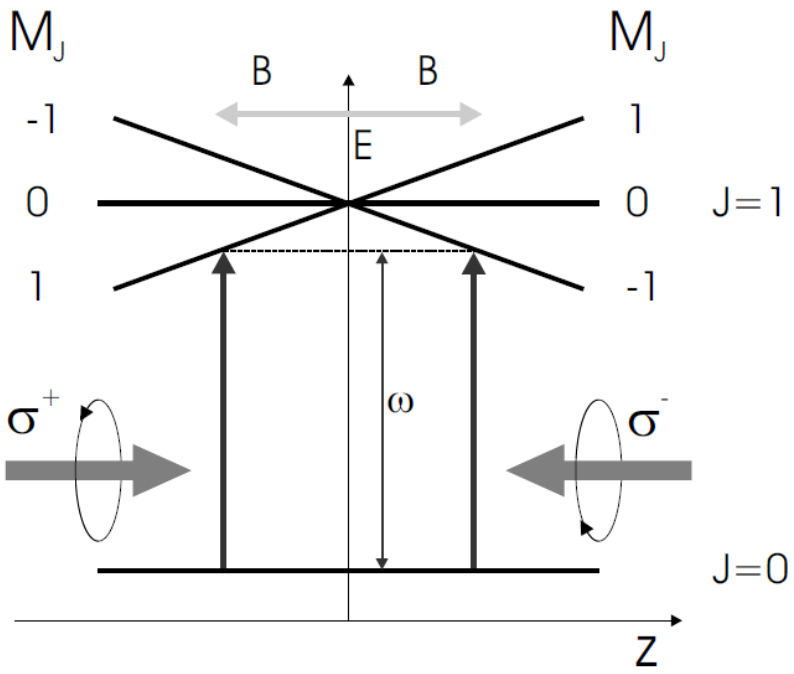

Figure 2.2 Explanation of the Zeeman trapping effect. An energy level diagram for an atom in a linear magnetic field gradient. The atom has a ground state $\mid g >$ with angular momentum quantum number $J = 0$. The excited state $\mid e >$ has $J = 1$ and thus three degenerate magnetic sub-levels $M_J = 0, \pm 1$. These levels have a linear Zeeman shift as a function of position. σ^- laser light only interacts with the $M_J = -1$ level and σ^+ only with the $M_J = +1$ level. With the laser configuration shown in the figure, the energy level of the atom comes closer to that of the red-detuned laser if the atom is farther away from the MOT. This results in a position dependent force that drives the atom towards the center of the MOT with damping coefficient κ. From [9].

Table 2.1 Properties of the trapping transition of ^{85}Rb [4].

quantity	symbol	value
wavelength	λ	780.24 nm
natural linewidth	Γ	5.98 MHz
saturation intensity	I_0	16.4 W m^{-2}
Doppler temperature	T_D	142.41 μK
ionization wavelength	λ_0	479.06 nm

Selection rules dictate that σ^+ polarized laser light can only interact with the $M_J = +1$ level, and σ^- light only with the $M_J = -1$ level. If the direction where the $M_J = -1$ level is lowered in energy is the opposite direction as where the σ^- laser beam is propagating, the atoms moving outside of the center are pushed back. The opposite side then has a lowered $M_J = +1$ energy level and an opposite laser beam of σ^+ light. The combination of the lasers and the magnetic quadrupole thus create a cooling and trapping mechanism.

If the Doppler and Zeeman shifts are both small, the force an atom experiences in a MOT can be expressed as [13]:

$$\mathbf{F_{MOT}} = -\alpha\mathbf{v} - \kappa\mathbf{r}, \tag{2.4}$$

where κ is the damping coefficient for the position $\mathbf{r}$ of the atom with respect to the center of the MOT.

2.1.3 Rubidium

The atom that is used in the MOT in the group is ^{85}Rb. The properties of this atom relevant to the MOT are given in table 2.1. The density of the MOT is about $n_a = 10^{16}$ m^{-3} and has an rms radius of $\sigma_a = 1$ mm.

The used notation here for energy levels in the atom is $NL_{J,F}$, where N is the principal quantum number and L is the angular quantum number indicated by a shell-letter (S, P, D, ...). J is the angular momentum quantum number including electron spin S ($J = L + S$) and F is the total angular momentum quantum number including nuclear spin I ($F = J + I$). The nuclear spin is responsible for hyperfine splitting. In Figure 2.3, the separate F-levels are indicated for the relevant energy levels in ^{85}Rb. The trapping and cooling transition for ^{85}Rb is from the $5s_{\frac{1}{2},3}$ to the $5p_{\frac{3}{2},4}$ state [4]. This transition is excited by a 780 nm diode laser (trapping laser). The trapping laser can also excite the $5p_{\frac{3}{2},3}$ state off-resonance. This state can decay back to the $5s_{\frac{1}{2},2}$ state, which cannot be excited again by the trapping laser. Therefore, an additional diode laser is employed (repump laser) to pump the $5s_{\frac{1}{2},2}$ state back to the $5p_{\frac{3}{2},3}$ state.

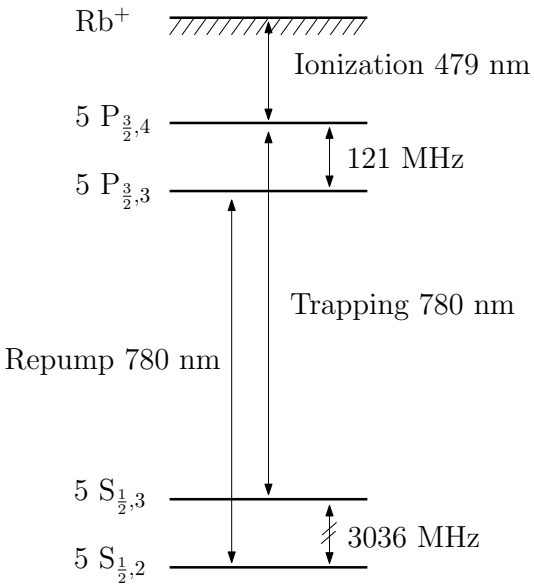

Figure 2.3 Energy level scheme (not on scale) of Rb showing the relevant hyperfine splitted levels of $5s_{\frac{1}{2}}$ and $5p_{\frac{3}{2}}$. The trapping laser and repump laser transitions are also indicated, as well as the ionization threshold. From [9].

2.1.4 MOT Setup

The MOT is created in a vacuum chamber. The pressure inside the chamber is in the order of 10^{-8} mbar, which is achieved with a turbo and an ion-getter pump. This low pressure is needed for the MOT to operate, because it reduces losses from elastic and inelastic collisions with background particles. The Rb is loaded from an ampul connected to the vacuum chamber. The cell is heated just above room temperature so a very small amount of Rb evaporates in time, enough to sustain the background gas that can be trapped and cooled by the MOT. The amount of trapped atoms can be controlled by setting the Rb temperature in the ampul.

The trapping laser is a cw 780 nm diode laser (Toptica DLX) that operates at 900 mW. The laser frequency is stabilized by modulation transfer spectroscopy, described in [14]. Beam splitters are used to split the laser in six beams. They are directed with mirrors so that they enter the vacuum chamber from six sides.

The repump laser is another cw 780 nm diode laser (Toptica DL 100) that operates at 100 mW and is slightly detuned with respect to the trapping laser. The frequency stabilizing was done with saturated absorption spectroscopy, described in ref. [15]. A new system locks the repump laser to the trapping laser with a phase-locked loop feedback system, which employs the small difference in frequency of $\nu_\delta = 2915$ MHz between the two transitions in Rb, described in [14]. This last system was installed after the

experiments were performed that are the subject of this thesis.

The MOT magnetic quadrupole consist of two coils both with 4 wires. The coils have a radius of 72 mm and are distanced 66 mm apart, with the MOT in the center. A typical current of $I_1 = 175$ A runs through the coils, which are water cooled.

The MOT is monitored by a calibrated photodiode, which records part of the fluorescent light from the trapping and cooling process exiting the vacuum chamber through one of the windows. This gives an measure for the MOT density. Two CCD cameras monitor the size and position of the MOT. They can also be used to check the Gaussian MOT density profiles in all directions.

2.2 Ionization and Acceleration Process

Three stages can be identified in the ionization and acceleration process of an electron bunch from the MOT, illustrated in Figure 2.4. First, Rubidium atoms are trapped and cooled in the MOT. Second, the cw 780 nm trapping laser is temporarily switched off, long enough so that most atoms relax back to their ground state. Another laser beam from the same cw 780 nm laser (excitation laser) is switched on and creates a small cylinder of excited $5p_{\frac{3}{2},4}$ atoms. A pulsed 480 nm laser beam (ionization laser) then ionizes the Rb atoms and creates a cloud of cold electrons. The ionization beam is orthogonal to the excitation beam, so that a chosen ionization volume can be created by controlling the overlap of the laser beams. Third, electrons are accelerated by means of an applied electric field. Electrons and ions are pulled out of the MOT in opposite directions.

2.2.1 Ionization

For ionization of Rb just above threshold, a tunable pulsed dye laser is used (Quanta-Ray PDL3). It is operated with Coumarin 480 nm dye, giving a tunable wavelength range of about $\lambda = 470 - 490$ nm. This is close to the ionization threshold of the excited $5p_{\frac{3}{2},4}$ Rb atoms of $\lambda_0 = 479.06$ nm. The dye laser is pumped by a 10 Hz Nd:YAG laser. The rms laser pulse length is $\sigma_t = 2.5$ ns with a bandwidth of 2 GHz and a pulse energy in the mJ range [16]. A part of the laser intensity is split off from the main beam and guided towards a wavemeter (LM-007 Lambdameter) to measure the exact wavelength with sub-ångström resolution.

The sizes of the excitation and ionization lasers are determined from calibrated CCD cameras that record the spot size of both lasers at a position equal to the center of the MOT. Photodiodes are employed to monitor the intensity of both lasers and to detect the moment of ionization in time.

The UCP volume can be characterized by three Gaussian distributions

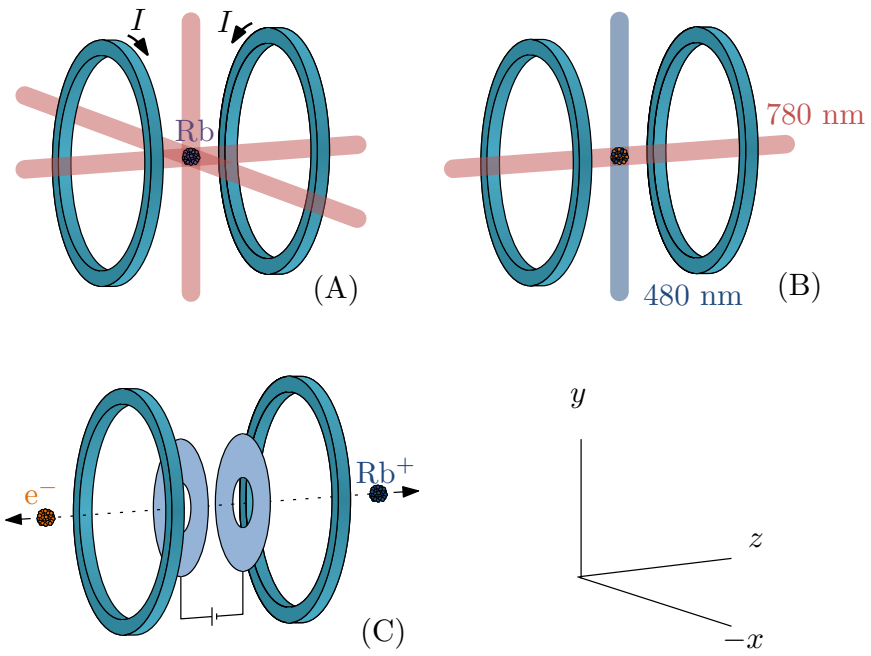

Figure 2.4 Electron bunches from an UCP. Rb atoms are cooled and trapped by a MOT (A). They are excited by a 780 nm cw laser (horizontal beam) and ionized by a 480 nm pulsed laser (vertical beam). The lasers are orthogonal to each other and their overlap determines the ionization volume (B). The created electrons and ions are accelerated by the electric field in opposite directions (C).

in the x, y (transversal) and z (longitudinal) directions. The z size of the plasma is completely determined by the excitation laser, and the y size completely by the ionization laser, both in the center of the MOT. The UCP rms size σ_x in the x-direction of the plasma follows from a multiplication of the two Gaussian laser profiles and is:

$$\sigma_x = \sqrt{\frac{1}{\frac{1}{\sigma_{ext,x}^2} + \frac{1}{\sigma_{ion,x}^2}}}, \tag{2.5}$$

where $\sigma_{ext,x}$ and $\sigma_{ion,x}$ are the rms sizes of the excitation and ionization laser in the x-direction in the center of the MOT, respectively. The rms sizes of the electron bunches are typically 15-50 μm in the experiments in this thesis.

The ionization process gives momenta to the e^- and Rb^+ particles that is equal in size, but opposite in direction. The mass of the Rb^+ ion is $m_i = 1.6 \cdot 10^6 \cdot m_e$. The kinetic energy that both particles receive from the ionization process is $p^2/(2m)$, which shows that virtually all the energy of the photon is transferred to the electron.

The relevant energy levels of the ionization process are shown in Figure 2.5. The figure also shows the excess energy an electron receives from the ionization process. The excess energy from the ionization photon E_λ is the difference between the ionization threshold of Rb and the photon energy:

$$E_\lambda = hc\left(\frac{1}{\lambda} - \frac{1}{\lambda_0}\right), \tag{2.6}$$

where h is the Plank constant and λ_0 the ionization threshold wavelength. Thus, by tuning the wavelength of the ionization laser, the excess energy of the electrons can be set.

2.2.2 Acceleration

Electron bunches created from the MOT are accelerated within a specifically designed accelerator structure, described in ref. [17] and illustrated in Figure 2.6. It consists of an outer conductor, which is grounded, and an inner conductor, which has a negative voltage applied to it to accelerate electrons. The conductors are separated by glass and the total structure has openings to allow the entrance of all the laser beams. The accelerator can sustain up to 30 kV acceleration voltage over a distance of 27 mm. This means the field strength is $\mathcal{F} = 37$ V/m per applied V acceleration voltage. The MOT is in the center of the accelerator structure, which means that electrons can achieve a maximum energy of 15 keV in this setup. In the experiments described in this thesis, energies are typically in the 1.5 - 3.0 keV range, for which a 6 kV power supply was used.

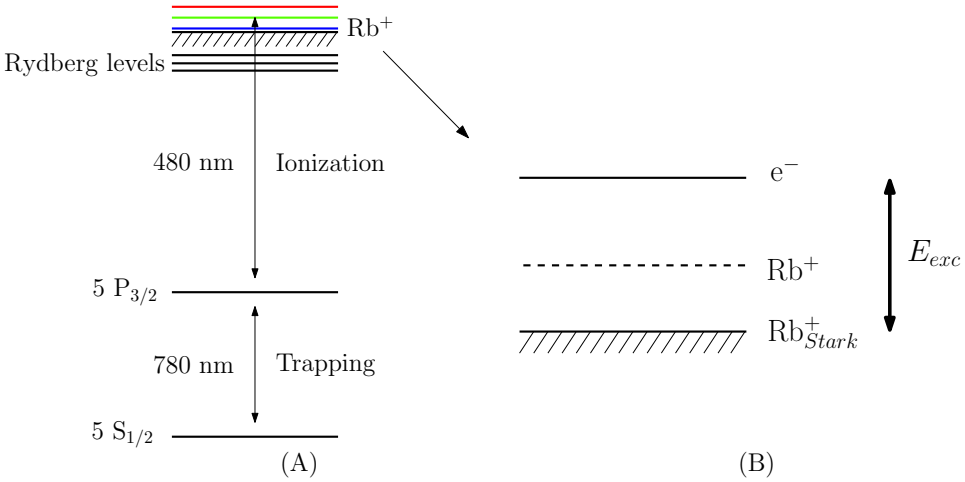

Figure 2.5 (A) Ionization scheme of Rb. A 780 nm cw diode laser excites the atom to the $5p_{\frac{3}{2},4}$ state. A 480 nm pulsed dye laser ionizes the atom. Indicated are some ionization levels in the continuum above threshold (colored lines) and Rydberg atom levels just below threshold (black lines). (B) Excess energy of an electron ionized just above threshold. If an electric field is present, the ionization threshold is lowered from the field free Rb^+ to the Stark shifted Rb^+_{Stark}. The Stark shift thus increases the excess energy of an electron.

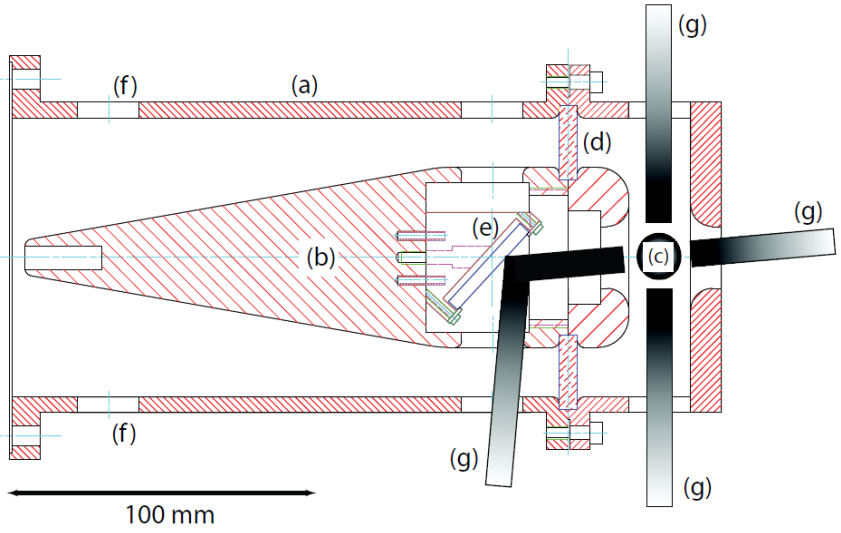

Figure 2.6 Technical drawing of the accelerator (cross section): (a) outer conductor, (b) inner conductor, (c) acceleration point, (d) glass ring, (e) mirror, (f) pumping holes, (g) laser beams. From [17].

The electric field has an effect on the ionization process. The electron and ion core are together an electric dipole, which is influenced by the local electric field strength $\mathcal{F}$. It effectively lowers the ionization threshold with the so-called Stark shift, indicated also in Figure 2.5. The excess energy an electron now gains increases with respect to Eq. 2.6 with [18]:

$$E_{Stark} = 4Ry\sqrt{\frac{\mathcal{F}}{\mathcal{F}_0}}, \tag{2.7}$$

where $Ry = 13.6$ eV is the Rydberg constant and $\mathcal{F}_0 = 5.14 \times 10^{11}$ V/m is the atomic unit of electric field strength.

The total excess energy of an electron is given by combining Eqs. 2.6 and 2.7:

$$E_{exc} = E_\lambda + E_{Stark}. \tag{2.8}$$

It does not follow from this equation how the momenta of the electrons in three directions are distributed. The momentum distribution is the subject of Section 4.1.

In Chapter 4, experiments with two different ionization schemes are presented. One ionization scheme of Rb is photoionization in a DC electric field. The electric field is constantly on during experiments. Electrons with $E_{exc} > 0$ are accelerated immediately, which means the ionization laser pulse length of $\sigma_t = 2.5$ ns is equal to the electron bunch length in the longitudinal z-direction. These are very long pulses compared to the desired $\sigma_t = 1$ ps for single-shot UED. However, the long pulse lengths ensure that space charge forces are not important for the created electrons, which is a useful condition for experiments. Experiments with this ionization scheme are described in Section 4.1.

Another ionization scheme of Rb uses pulsed electric field-ionization of Rydberg atoms. In this case, the Rb atom is not ionized, but excited by the 480 nm laser just below ionization threshold energy. The energy levels there are called Rydberg states, which are states in which the outer electron is very far away from the atom core and its other electrons. The corresponding energy levels are characterized by the principal quantum number n, with energy $-Ry/n^2$. These Hydrogen-like atomic systems are used in many fundamental physics experiments, because of their long lifetime and sensitivity for electric fields [19].

The excitation to a Rydberg state is done while the electric field is off. After excitation, an electric field pulse field-ionizes the Rydberg atoms and creates very short temporal electron bunches. In principle, bunch lengths of $\sigma_t = 50$ ps can be reached with pulsed field-ionization in the current setup. However, until now $\sigma_t = 0.85$ ns is the minimal pulse length that is measured [4]. Measurements of the source temperature in Section 4.2 are performed with this ionization scheme.

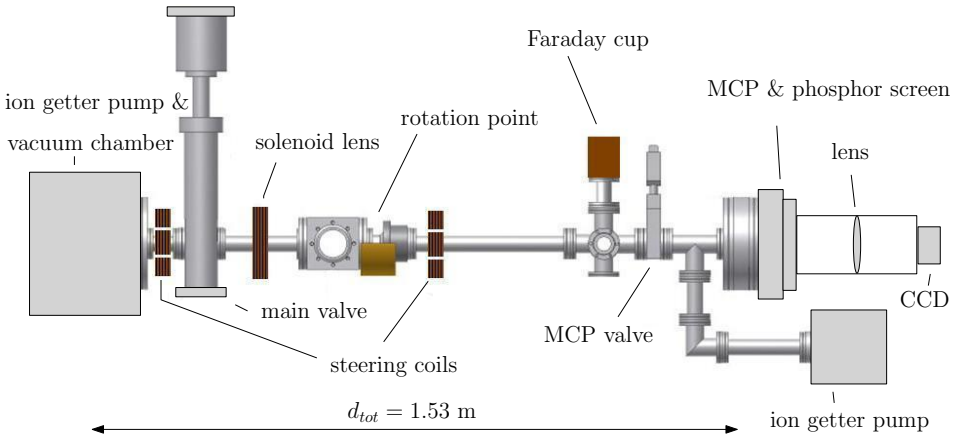

Figure 2.7 The beam line of the UCP setup with the main components indicated.

2.3 Beam Line and Detector

Electrons created in the MOT are accelerated through a beam line towards a detector. The detector consists of four components. First electrons hit a micro-channel plate (MCP), where multiple electrons are emitted per incident electron. After the amplification by the MCP, electrons are accelerated towards a phosphor screen by an applied electric field. Here, photons are emitted by electrons hitting the screen. The light from the phosphor screen is imaged by a lens on a CCD camera. The whole setup is shown in Figure 2.7. The beam line and detection system are described in more detail below.

2.3.1 Beam Line

The beam line consists of mainly 40CF (40 mm diameter) stainless steel pipes. Two magnetic steering coils and a magnetic focussing solenoid are clasped around the pipes. They are there to control the direction and size of electron bunches, respectively. A complete overview of the lenses in the setup and their properties relevant for electron trajectories is given in Section 3.2.

Small external magnetic fields are a huge problem when controlling the trajectory of electrons. To illustrate this, the cyclotron radius r_c of an electron moving with a longitudinal velocity corresponding to acceleration energy U, perpendicular to a magnetic field B is:

$$r_c = \frac{\sqrt{2m_e U}}{eB}. \tag{2.9}$$

Typical acceleration energies in experiments are $U = 1$ keV. Electrons move in the earth magnetic field of about $B = 50$ μT that is perpendicular to

the beam line. This then results in $r_c = 2$ m, while the detector is at $d_{tot} = 1.53$ m. Therefore, even with the earth magnetic field alone, it is already very difficult to direct the electrons through the 40 mm beam line using only magnetic steering coils. Additional magnetic field sources can be magnetized screws, bolts and other equipment near the setup.

As a solution, an earth magnetic field compensation system has been built around the setup. It consists of copper wires mounted on both sides of the beam line at a distance of roughly $d = 0.2$ m. A current of about $I = 6$ A is run through the wires, which cancels the B-field on the axis of the beam line over a large part of the setup. Together with the magnetic steering coils, it is possible to direct the electron bunches to the detector without losing parts of the bunch to wall collisions during its travel through the beam line.

A rotation point is included in the beam line, to make the whole setup less rigid and to enable the precise alignment of the detector with respect to the center of the vacuum chamber. A bellows allows small angles between the two pipes that are connected at the rotation point. This bellows would normally completely contract under vacuum, except that an outer bearing is there to prevent that.

Not far from the detector is a Faraday Cup, a small copper plate inside beam line vacuum that is connected to a current amplifier outside the setup with a copper wire. The Faraday Cup can be rotated into the path of the electron bunches. The charged particles that hit it go through the amplifier and the integrated time-signal of the current results in a voltage that is representative for the bunch charge. The Faraday Cup amplifier has a response of 3.5 fC/V, meaning each output of 1 V represents 3.5 fC bunch charge. The charge Q has been determined for ion and electron bunches created with the same ionization conditions, but for different acceleration energies. The results of 10 averaged bunch charges are shown in Figure 2.8.

The figure shows a negative charge for electrons and a positive charge for ions, what is expected. For low energetic particles, the signal becomes smaller. At these low energies ($U < 500$ eV), the electron bunches are blown up so much in size that they do not reach the Faraday Cup. This is less of a problem for ions. At high negative and positive V_{acc}, particles are energetic enough to create secondary electrons that scatter from the copper plate. This process adds a positive current, so the electron signal decreases and the ion signal increases.

For both the electrons and ions, a small plateau can be seen in the dependency on V_{acc}. It represents the energy range of the particles where the material effects play almost no role. The plateau is equal in size for both particles, which corresponds to average bunch charges of $Q = 2.3$ fC. It runs approximately from $V_{acc} = 1.0 - 3.0$ kV for ions and from $V_{acc} = 0.8 - 1.6$ kV for electrons. For a charge calibration of other measurement systems, the measured dependency on the acceleration voltage is an important factor

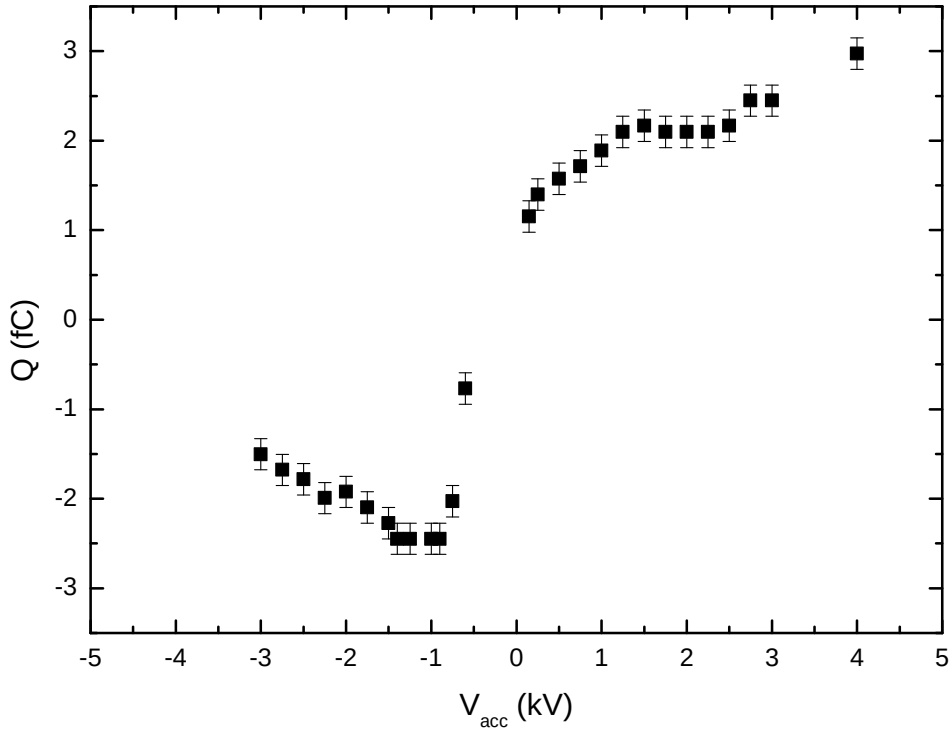

Figure 2.8 Faraday Cup integrated current signal as a function of acceleration voltage. Both for ion (positive V_{acc}) and electron (negative V_{acc}) bunches the charge has been measured. The measurements are averaged over 10 bunches.

to take into account.

A charge calibration of the detector has been performed. Both the integrated intensity of the images on the CCD camera and the current signal on the oscilloscope were compared to the measurements with the Faraday Cup. For several electron energies and MCP voltage settings, the charge was calibrated and these values were used in the charge measurements described in Section 4.2.

2.3.2 Detector

Electron bunches that reach the end of the beam line hit a MCP detector, which has a diameter of 40 mm. The MCP is made by Photonis and it consists of two glass plates. Within are millions of small glass channels of 5 μm diameter, distanced 8 μm apart. When an electron enters a MCP channel, it hits the wall of the channel because the channels are placed under an angle with respect to the normal of the plane of incidence. The impact of the electron starts a cascade of electrons that are accelerated through the channel because of an applied voltage between the front and the back of the MCP.

In the UCP setup, even a double MCP is used with another microchannel plate placed behind the first. Typically, the front plate was grounded and the back plate was put a +2 kV, the maximum setting for the MCP. This gives an amplification of about 10^7, allowing detection of single electrons hitting the detector.

An ion getter pump is located close to the MCP together with a valve to separate it from the rest of the setup. This way, the MCP can be kept under vacuum if parts of the beam line need to be replaced. The MCP damages quickly if exposed to atmospheric pressures.

Placed behind the MCP is phosphor screen that emits photons when hit by electrons. The active material in the phosphor screen is ZnCdS:Ag, which emits photons in the spectrum between 470 and 670 nm, with a maximum intensity at 550 nm [16].

The light is imaged on a CCD camera by a positive lens. The CCD camera pixel size is 12 μm and the magnification of the lens is 1.8. This means that each pixel on the CCD represents 22 μm on the detector, which is larger than the channel size of the MCP. This is the minimum resolution obtainable for measuring spot sizes.

However, a measurement with a pinhole in front of the detector showed that 95 μm is the smallest spot that could be measured, so that is used as a minimal resolution in this report. Another practical consideration is the 'binning' of CCD camera pixels during measurements. A much used binning of 10 makes the CCD chip read out 10×10 pixels as one, greatly reducing the time needed for experiments. The resolution then also increases by a factor of 10 to 220 μm, but this is acceptable for most measurements.

2.4 Software for Controlling the Setup

A large part of the setup is controlled by software to synchronize timings, change parameters and measure variables. The software control system is illustrated in Figure 2.9.

The software basically consists of two main programs. The first program controls the nanosecond timings of the lasers and acceleration field for the creation of electron bunches. The repetition rate of this process is limited by the ionization laser, which can run at a maximum of 10 Hz. The software works with a dedicated hardware client made in the group, the Programmable Pattern Generator (PPG). It runs on a 100 MHz clock, meaning a time resolution of 10 ns. The PPG allows the software to change setup parameters without disturbing the timing cycle, so large measurement series can be automated.

The second program, the Scan Controller, synchronizes the measurement on a second timescale. It can vary parameters in the setup over time, for example the ionization laser wavelength, to create measurement series. It does that by controlling various hardware clients, for example the PPG. It also connects to multiple dedicated acquisition clients that read out various settings and signals. This includes oscilloscope signals that record the current from the MCP and bunch size images recorded on the CCD camera. All the data is collected per measurement and stored in one place.

The ionization laser wavelength can be set by a stepping motor. The motor can slightly alter the size of the cavity of the laser, so that another wavelength becomes resonant. The wavelength of the laser is read out by a wavemeter (LM-007 Lambdameter) that uses gratings of different sizes to determine it to high precision. Software has been made to set the ionization laser wavelength while receiving feedback from the wavemeter. If a wavelength is set, the program sends a pulse train signal to the stepping motor, which then takes an amount of steps. The maximum amount of steps that can be set in a single pulse train corresponds roughly to a nm. After the pulse train and a small delay, the software polls the wavemeter and reads out the actual wavelength. The process is then repeated until convergence is reached.

The software controls the wavelength down to steps of 0.01 nm, which is precise enough to tune the laser to Rydberg transitions in the Rb atom. It is also possible to put in Rydberg state quantum numbers. The program then calculates the wavelength corresponding to the transition and sets the laser accordingly. It can connect to the Scan Controller software, so a measurement series can also include the variation of ionization laser wavelength.

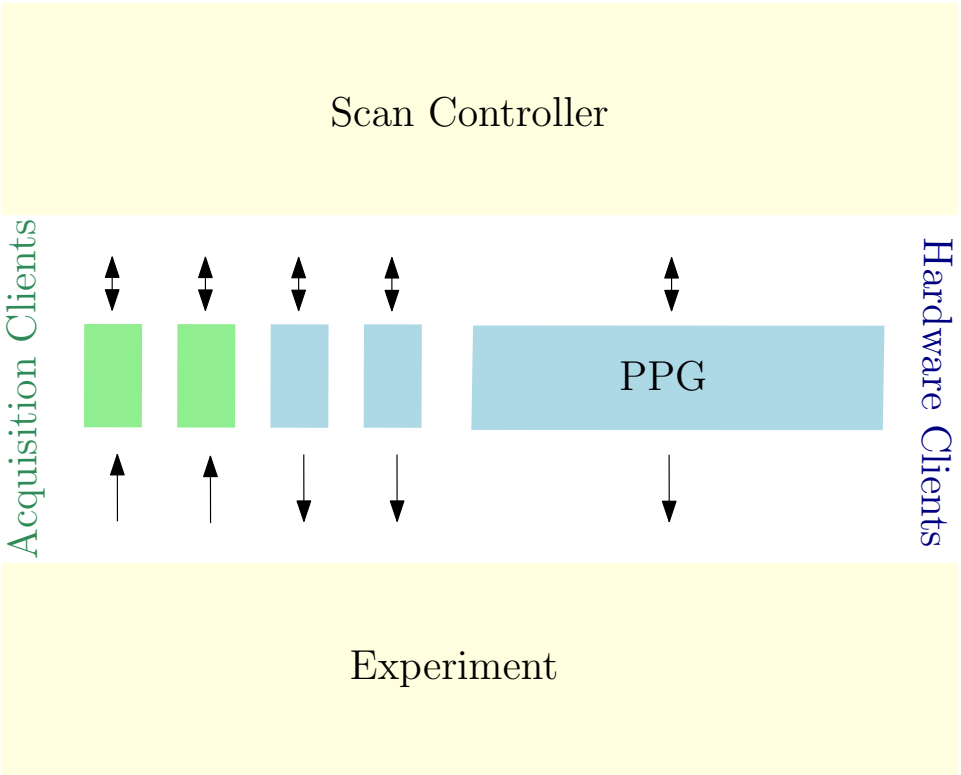

Figure 2.9 The software control system of the setup. Green and blue colors indicate acquisition and hardware clients, respectively. The PPG controls the timings relating to the creation of electron bunches in the setup. The Scan Controller runs the experiment and is able to set experimental parameters and read out measured variables from the various clients.

Chapter 3

Electron Trajectory Model

In this chapter, an electron trajectory model is presented of the UCP setup. From this model follows a method to calculate the transverse temperature of electrons in the MOT analytically. The model is used to characterize the setup and design a magnetic solenoid lens. GPT simulations of the particle trajectories are used to extract a temperature from the data analysis.

The UCP setup described in Chapter 2 basically starts with a MOT in an accelerator structure. Then a beam line follows where electron bunches drift and are focussed and defocussed by electromagnetic lenses. They finally reach a detector which records the transverse sizes and longitudinal intensity of the bunches. In Section 3.1, a quantative model for particle trajectories is introduced using optical transfer matrices. The electric and magnetic lenses in the setup are the subject of Section 3.2.

In past experiments [4], electron bunch sizes were measured on the detector that was at the end of the vacuum chamber, 0.30 m from the MOT. Electron energy was varied and the electron trajectory model was used to obtain transverse electron temperatures down to 10 K. However, if lower temperatures need to be measured, the length of the beam line at some point limits the temperature resolution of the system. This is because over such a distance the bunch sizes change to little to see a temperature effect. It means to measure down to $T = 1$ K, the beam line needs to be extended. This has been done for new measurements described in this thesis, giving the setup a total length of 1.53 m.

When the electron energy is increased, a higher acceleration voltage is needed. As seen in Section 2.2, this gives rise to a higher Stark shift in the Rb ionization threshold, which increases the excess energy and thus the temperature of the electron bunch. This means you cannot measure temperature independently by using electron energy as a scanning parameter. A magnetic solenoid lens has been designed for which the focal length can be independently changed, resulting in a new method for measuring temperature. The longer beam line and magnetic solenoid lens are the subject

of Section 3.3.

The goal in experiments is to measure the transverse electron temperature. To obtain a single temperature, a series of measurements or a so-called 'waist scan' was done where the current of the magnetic solenoid lens was varied. Measurements consisted of electron bunch intensity images recorded on an CCD camera that was placed after a MCP and phosphor screen detection system. Also, time-signals of the MCP current and the ionization laser intensity were both recorded on an oscilloscope. Analysis methods of this data with Matlab scripts and GPT simulations are described in sections 3.4 and 3.5, respectively.

3.1 Optical Model of the Setup

In this section, the particle trajectories in the setup are described in terms of an analytical model. This model is analog to an optical model in which ray tracing is employed [16, 20, 21]. Ray tracing describes the position and angle of a light ray or a charged particle as a function of focal lengths and drift spaces. Lenses alter the path of light rays or charged particles. For an optical lens the refraction index of the material determines the focal length, in charged particle optics the focal length is determined by local electric and magnetic fields. Both optical and charged particle systems can be described by transfer matrices that represent lenses and drift spaces.

For charged particles, these matrices relate in 1D the final position x_f and angle x'_f of a particle to the initial position x_i and angle x'_i. The angle with respect to the beam line for a single particle is:

$$x' = \frac{p_x}{p_z}, \tag{3.1}$$

where p_x is the x-momentum (in a transverse direction) and p_z the z-momentum (in the longitudinal acceleration direction).

A lens with focal length f is represented by:

$$\mathcal{M}_{\mathcal{F}} = \begin{pmatrix} 1 & 0 \\ -\frac{1}{f} & 1 \end{pmatrix}. \tag{3.2}$$

A drift space d is represented by:

$$\mathcal{M}_{\mathcal{D}} = \begin{pmatrix} 1 & d \\ 0 & 1 \end{pmatrix}. \tag{3.3}$$

A complete beam line transfer matrix $\mathcal{M}$ can be described by matrix-multiplying these matrices:

$$\mathcal{M} = ...\mathcal{M}_{\mathcal{D}3}.\mathcal{M}_{\mathcal{F}2}.\mathcal{M}_{\mathcal{D}2}.\mathcal{M}_{\mathcal{F}1}.\mathcal{M}_{\mathcal{D}1}, \tag{3.4}$$

where the numbered focal and drift matrices are multiplied in the reverse order as they are seen by the particle going through them. So in Eq. 3.4, particles first travel through drift space d_1, then through lens with focal length f_1, etc.

This results in:

$$\begin{pmatrix} x_f \\ x'_f \end{pmatrix} \equiv \mathbf{f} = \mathcal{M}\mathbf{i} \equiv \begin{pmatrix} A & B \\ C & D \end{pmatrix} \begin{pmatrix} x_i \\ x'_i \end{pmatrix}, \tag{3.5}$$

where A, B, C and D are the matrix coefficients of the total beam line.

With these focus lengths and the appropriate drift spaces, the final rms spot size σ_{x_f} of the whole electron bunch can be expressed in terms of the transfer matrix coefficients A and B, the initial rms spot size σ_{x_i} and the initial rms divergence $\sigma_{x'_i}$ [4]:

$$\sigma_{x_f}^2 = A^2\sigma_{x_i}^2 + B^2\sigma_{x'_i}^2. \tag{3.6}$$

The proof of this is given in ref. [16]. A rms spot size is always a positive quantity and is a measure for the area in which a part of the particles fall. In the case of a Gaussian spatial distribution of electrons, σ is the standard deviation of the distribution and $\sqrt{2\pi}\sigma$ represents the region in which 68 % of the particles are located.

The creation of electrons in the MOT is done by photoionizing them just above threshold with the ionization laser. As mentioned in Section 2.2, they gain an excess energy E_{exc} from this process. Note that the electron bunch is accelerated in longitudinal direction to kinetic energies U orders of magnitudes higher than E_{exc}.

In a transverse direction (x or y), only E_{exc} is of importance and the momentum of the electrons can be expressed purely in terms of temperature. From Eq. 1.3, $\sigma_{p_{xi}} = \sqrt{m_e k_B T}$. In the longitudinal direction, only the acceleration energy U is significant. The average momentum p_{z_i} of electrons follows from equating U to the kinetic energy $p_{z_i}^2/(2m_e)$ (and ignoring the temperature):

$$p_{zi} = \sqrt{2m_e U}. \tag{3.7}$$

From Eq. 3.6 and $\sigma_{x'_i} = \sigma_{p_{xi}}/p_{zi}$ then follows:

$$\sigma_{x_f}^2 = A^2\sigma_{x_i}^2 + B^2\frac{k_B T}{2U}. \tag{3.8}$$

This means that if the initial bunch size and the energy of the particles is known, the temperature can be determined if the final bunch size is measured as a function of a beam parameter. In the experiments described in Chapter 4, this beam parameter is the current through a magnetic solenoid lens that is the subject of Section 3.3.

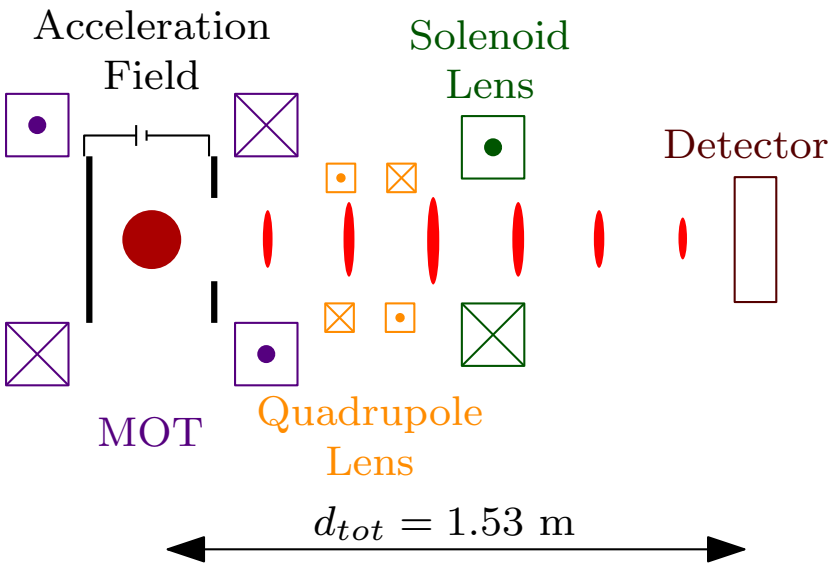

Figure 3.1 Schematic overview of the beam line lenses. Electron bunches (bright red) are created in the MOT (dark red Rb cloud and purple solenoids), accelerated (black plates), focussed in x and defocussed in y (orange quadrupole lens) and finally focussed (green solenoid lens) on the detector (brown).

3.2 Electric and Magnetic Lenses

In the UCP setup, several electromagnetic lenses can be distinguished, see Figure 3.1. They are explained below in more detail and their relevant characteristics are given in table 3.1.

There are differences between ions and electrons when they interact with electric and magnetic lenses. The electric force on a charged particle is [22]:

$$\mathbf{F_E} = q\mathbf{E}, \tag{3.9}$$

where q is the charge of the particle and $\mathbf{E}$ is the electric field. This means electrical forces are equal in magnitude for electrons and ions. The direction is different because of the opposite charges of the particles.

The magnetic force on a particle is [22]:

$$\mathbf{F_B} = q\mathbf{v} \times \mathbf{B}. \tag{3.10}$$

The velocity for accelerated particles in the longitudinal direction is $v_z = \sqrt{2U/m}$, with m the mass of the particle. A Rb ion has a mass that is $m_i = 1.6 \cdot 10^6 \cdot m_e$, meaning that magnetic forces are 7.9×10^{-4} times weaker for ions. In the setup, this means that magnetic forces can be neglected for ions, but are quite important for electrons.

Table 3.1 Electric and magnetic lenses in the UCP setup.

lens	position (m)	focal length (m)
exit kick	0.010	-0.033
MOT	0.024	$+24$ [A^2 m / eV] $\cdot U$ / I^2
quadrupole (x)	0.250	$+8.7 \cdot 10^{-3}$ [m / eV$^{\frac{1}{2}}$] $\cdot U^{\frac{1}{2}}$
quadrupole (y)	0.250	$-8.7 \cdot 10^{-3}$ [m / eV$^{\frac{1}{2}}$] $\cdot U^{\frac{1}{2}}$
solenoid	0.530	$+2.1 \cdot 10^{-3}$ [A^2 m / eV] $\cdot U$ / I^2

3.2.1 Electrostatic Aperture Lens

The first lens the electrons encounter while travelling through the beam line is an electrostatic lens created effectively by the accelerator structure. The axial electric field in the accelerator is maximal in the center and it falls off towards the exit. This leads to a radial electric field. In the case of electrons, where the accelerator field in the positive z-direction has a negative gradient, the radial field points inward which leads to a negative lens effect. This type of lens is known as a electrostatic aperture lens [21]. The fieldmap of the accelerator has been modelled earlier [4] and from this an effective focal length could be determined (see table 3.1).

3.2.2 Magnetic Solenoid Lenses

The second effective lens is created by the MOT magnetic fields. The magnetic field coils in the setup are in the anti-Helmholtz configuration. They create the linear gradient in the center of the MOT needed for trapping, but also act as a solenoid lens for particles travelling in the longitudinal direction [16].

The fourth lens is also a magnetic solenoid lens, which is used as a scanning parameter for waist scan measurements in the photoionization experiments described in Chapter 4. The design and positioning of this lens is treated in Section 3.3.

The focal length of a magnetic solenoid lens is [21]:

$$f = \frac{4}{\int\limits_{-\infty}^{\infty} dz \left[\frac{qB_z(0,z)}{\sqrt{2\gamma^2 m_e U}}\right]^2}, \tag{3.11}$$

where γ is the relativistic factor and $B_z(0,z)$ is the on-axis magnetic field in the z-direction. In this case, $\gamma \simeq 1$ and $B_z(0,z)$ can be approximated by the on-axis magnetic field of a infinitely thin current loop:

$$B_z(0,z) = \frac{\mu_0 I}{2} \frac{R^2}{(z^2+R^2)^{3/2}}, \tag{3.12}$$

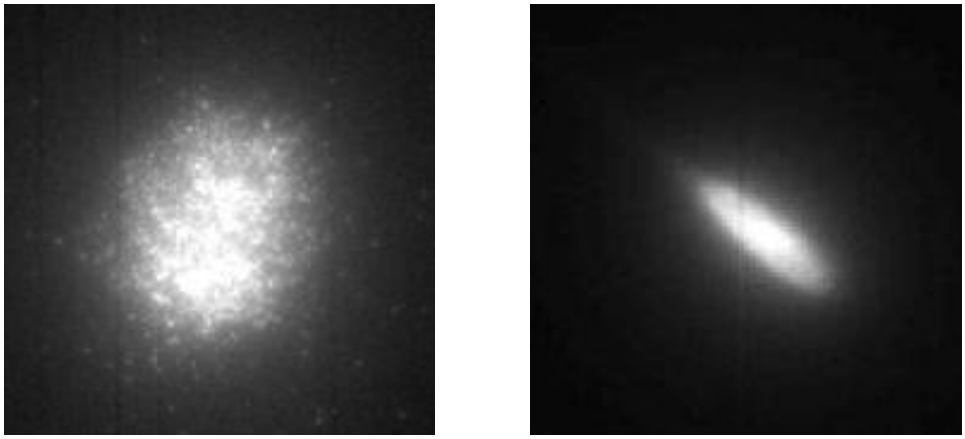

Figure 3.2 Particles detected on the MCP: a round ion bunch (left) and an elliptical electron bunch (right). Energies and settings are the same for both bunches. The ion spot has been scaled down relatively to the electron spot.

where μ_0 is the permeability of free space, I the current windings through the solenoid and R the radius of the solenoid. A solenoid acts as a positive lens for which the strength is dependent on the acceleration energy of the electrons. Therefore the focal lengths in table 3.1 are given as a function of acceleration energy U and current I through the solenoid.

A solenoid also introduces a rotation in an electron bunch, because of the magnetic forces that are present from the transverse velocities of the electrons and the longitudinal magnetic field. For a solenoid, the rotation α an electron bunch undergoes in a beam line with length d_{tot} is [4]:

$$\alpha \approx -\int_0^{d_{tot}} dz \frac{eB_z(0,z))}{\sqrt{8m_eU}}. \tag{3.13}$$

3.2.3 Magnetic Quadrupole Lens

As described in Section 2.2, electron bunches are ionized in the intersection of two lasers, creating an almost spherical bunch with Gaussian spatial distributions in all three directions. However, in the measurements described in Chapter 4, an asymmetry is visible when observing the spot size in both transverse directions. Figure 3.2 shows both an ion and electron bunch detected on the MCP for the same settings and particle energies. Notice the difference in shape: the ion bunch is almost round, while the electron bunch is clearly elongated in one direction. Besides that, the ion figure has been scaled down, so the difference in absolute size is even larger than shown.

The difference in absolute size of the bunches can be explained by the electric and magnetic fields that act as charged particle lenses. Ions are only influenced by the electric exit kick from the accelerator, acting as a negative

lens. Electrons also experience the magnetic positive solenoid lenses, which compress the bunch size. This results in the large ion spot shown in the figure as compared to the electron spot. The rotation of the electron bunch that can be seen in Figure 3.2 is due to the solenoid lenses, see Eq. 3.13.

However, the solenoid lenses cannot explain the difference in shape observed between ion and electron bunches. The ionization volume used for the spots shown in the figure is almost spherical, so the ion bunch has the shape that is expected. This means the elongation of the electron bunch is likely to be due to magnetic forces. A constant magnetic field like that of the earth deflects the entire bunch. Therefore, only a magnetic field gradient can explain a focussing or defocussing effect, because the forces then are position dependent within the electron bunch.

A candidate for generating this magnetic field gradient in the setup is a mirror inside the vacuum chamber. This mirror is about 30 mm from the beam line and is made of stainless steel, which can become magnetic over time. It takes a lot of time to pump the vacuum chamber down to the desired pressure again after it has been opened, which has until now prevented the further investigation of the mirror. However, the magnetic field source can be considered theoretically as a bar magnet. The magnetic field of a bar magnet can expressed as a multipole expansion, see ref. [22] for a detailed description. It suffices to say here that the first term is that of a dipole, which effectively deflects the whole electron bunch, and the second term is a quadrupole field. The rest of the terms are ignored.

The quadrupole field in both transverse directions is $B_x = Ky$ and $B_y = Kx$, where K is a linear gradient coefficient. The focal length of a quadrupole lens is [23]:

$$f_{\pm} = \pm \frac{\sqrt{2m_e U}}{e} \frac{1}{KL}, \tag{3.14}$$

where L is the length of the quadrupole and the $\pm$ indicates the difference in transverse direction, which is only a sign change. The force acting on electrons due to a dipole field and quadrupole field can be seen in Figure 3.3. The electrons are accelerated perpendicular to the plane shown, coming out of the figure. The dipole field results in a homogeneous field shift in one direction (x-axis). The quadrupole field results in a force acting inwards, or focussing, in the x-direction and outwards, or defocussing, in the y-direction.

The position of the quadrupole lens can be estimated as the position of the mirror, which is at 25 cm from the MOT. The product of KL determines the strength of the lens. Comparing measured waist scans (spot sizes vs. solenoid current) with the model from Section 3.1 for different electron energies, a value for KL is estimated, which is $KL = 0.39 \times 10^{-3}$ T. This translates into the focal lengths mentioned in table 3.1. Figure 3.13 in Section 3.5 shows how well the two transverse measured spot sizes on the detector can be understood with the inclusion of this lens in the analysis.

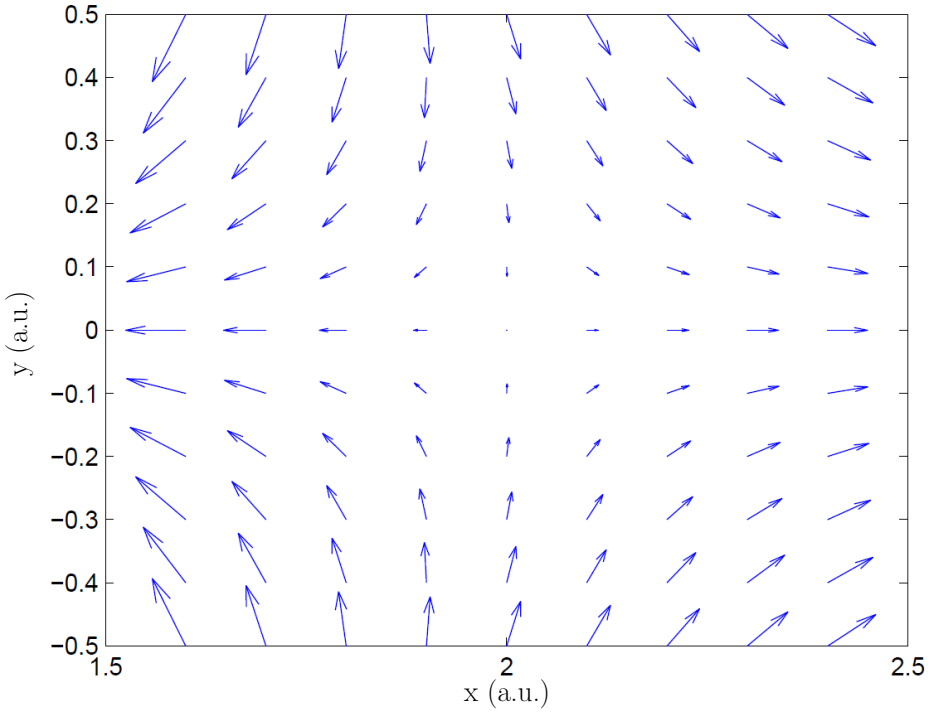

Figure 3.3 Force acting on electrons in a dipole and quadrupole magnetic field, with arbitrary position scales on the axes. Electrons are accelerated outwards from the plane depicted here.

3.3 A New Beam Line

The beam line lenses are schematically depicted in Figure 3.1. The two most important (strongest) lenses for the electron trajectories are the negative electric exit kick lens and the positive magnetic solenoid lens. Basically, a point source of electrons (≤ 50 μm) in the MOT is magnified with a factor ≥ 1 on the detector (transverse spot sizes $\sim$ 0.1 - 10 mm).

This system can be considered as a reverse telescope: instead of catching in a large area of light to look at a distant star with a high spatial resolution, this system blows up the initial object to create a high angular resolution. This can be seen in Eq. 3.6: a telescope makes the A-term of the image large (magnifying the initial object), while keeping the B-term small (optimizing sharpness of the image). In the UCP setup, the A-term must be as small as possible (reducing the effect of initial size) and the B-term as large as possible (increasing the effect of temperature).

If the temperature resolution needs to be increased, this essentially means smaller angles must be resolvable. This can be done by increasing the length of the setup. Because the setup still needs to be manageable as a table-top setup, an extension of the beam line could be realized up to

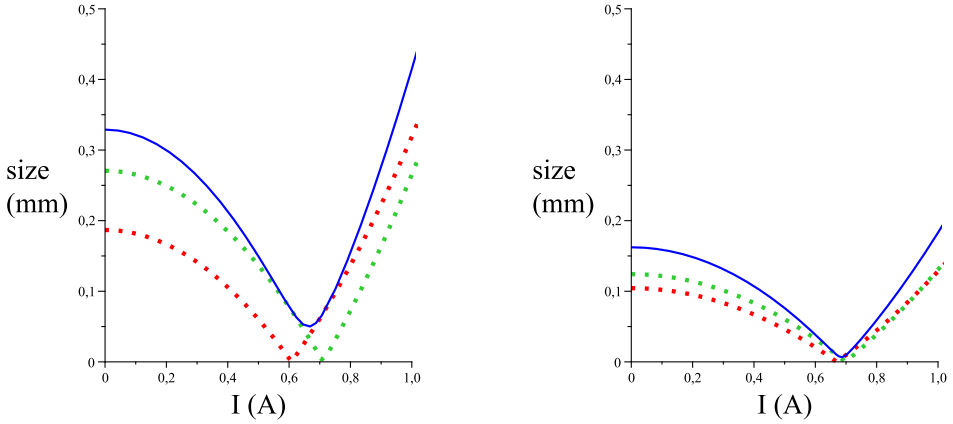

Figure 3.4 Absolute values of the initial spot size term $A\sigma_{x_i}$ (dotted red line) and the initial divergence term $B\sqrt{k_B T/(2U)}$ (dotted green line) as a function of lens current I. Typical values of $\sigma_{x_i} = 25$ μm, $T = 10$ K and $U = 2.1$ keV are used as an example. The total rms spot size is also indicated (solid blue line). This is calculated with Eq. 3.8. In Figure (a), the magnetic solenoid lens is at $d = 0.53$ m and in Figure (b) at $d = 1.28$ m. Axes in both graphs are identical.

1.53 m from the MOT center to the detector.

When the beam line is made longer, a positive lens is needed to focus electron bunches on the detector for energies above 1.1 keV. The most straightforward design is a magnetic solenoid lens, for which the focal length is tunable by changing the current through the windings, see Eq. 3.11. The lens must be on a position so that the best temperature resolution is created in the system. This idea is investigated with the analytical model from Section 3.1.

A typical temperature measurement consists of measuring spot sizes for about 20 different currents through the magnetic solenoid lens, resulting in a waist scan. From this waist scan, using both transverse spot sizes, the temperature is fitted to particle trajectory simulations in GPT. This procedure is described in Section 3.5. With the analytical model from Section 3.1, some predictions can be made about the measurements.

From Eq. 3.8, it can be seen that if there is a point $A = 0$, then the spot size is completely determined by the temperature. Also, if there is a point $B = 0$, then the source size completely determines the spot size on the detector. However, the absolute minimum spot size in a waist scan does not correspond to either $A = 0$ or $B = 0$. This is illustrated in figures 3.4a and 3.4b, for the lens positioned at $d = 0.53$ m and $d = 1.28$ m, respectively. The figures show both the initial position and initial angle term from Eq. 3.8, that together form the final rms spot size, which is also shown in the

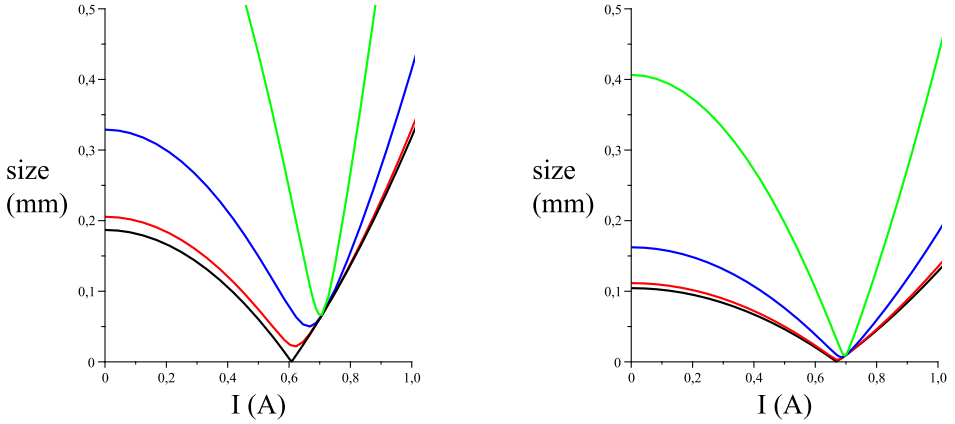

Figure 3.5 Spot size as a function of lens current. Temperature of 0 K (black), 1 K (red), 10 K (blue) and 100 K (green). In Figure (a), the magnetic solenoid lens is at $d = 0.53$ m and in Figure (b) at $d = 1.28$ m. Axes in both graphs are identical.

figure.

The distance $d = 0.53$ has been chosen because that is the minimal distance from the MOT that the lens can be positioned in the setup. This is because of the vacuum chamber and the valve that is behind it. The distance $d = 1.28$ is 25 cm from the MCP detector, so relatively far away from the chamber. What can be seen from the figures is that for the position close to the MOT, A and B coefficients are both larger than when the lens is close to the detector. This is where the minimum spot size on the detector is important. The minimal resolution on the MCP has been determined to be 95 μm. With the lens close to the detector, the minimum spot size falls well below that, something which decreases the accuracy of the measurements a lot. However, with the lens close to the MOT, the minimum spot size is about the size of the detector resolution, making it a good choice for placing the lens.

Figures 3.5a and 3.5b further illustrate the choice of positioning. For four different temperatures, 0 K, 1 K, 10 K and 100 K, the spot sizes have been plotted as a function of lens current. The difference in size between the curves for different temperatures is greater for the lens located closer to the MOT. This can be seen as a measure for the resolution. The conclusion is that the best place for the lens in the beam line is at $d = 0.53$ m.

For practical reasons, the solenoid is designed to create the desired magnetic field without generating too much heat and needing active cooling. A logical choice is to use copper for the windings, because of the low resistance. The amount of windings determines the current that a power source needs to supply. Too few windings mean a high current, which needs an expensive

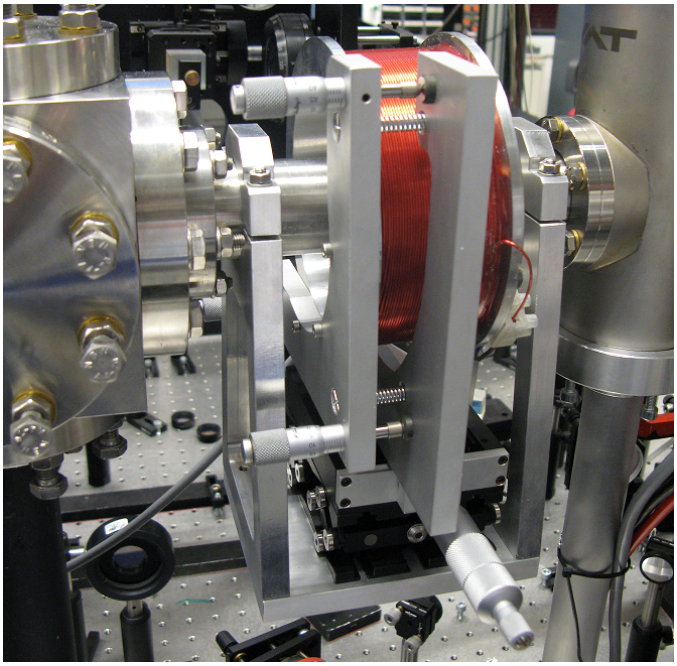

Figure 3.6 The magnetic solenoid lens mounted on the beam line. A horizontal and vertical stage enable the translation of the lens, the two ring mounts enable the rotation of the lens.

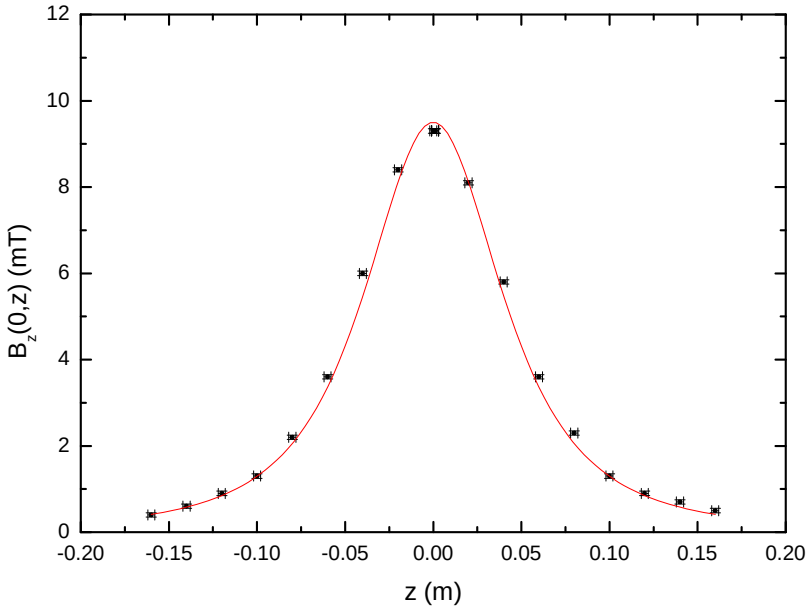

Figure 3.7 The black points represent the $B_z(0,z)$-field along the z-axis of the solenoid lens. The red line fit of $B_z(0,0)$ is with Eq. 3.12.

power supply, while too many windings give a low current, sensitive for noise with standard power supplies. In this case, $N = 200$ windings was chosen, so the lens can operate between $I = 0-5$ A. In the experiments done, mostly $I = 0 - 2$ A was chosen for electron energies between $U = 1.0 - 3.0$. The full current range enables waist scan measurements up to $U = 40$ keV.

The solenoid is placed in a mount that enables the position and orientation of the lens with respect to the beam line to high precision. Four μm-screws control both transverse positions and both angles of the lens with the transverse plane of the beam line. The lens is shown in Figure 3.6.

A magnetic field measurement of the lens has been performed to check the desired behaviour. Figure 3.7 shows the $B_z(0, z)$-field on the z-axis. The on-axis $B_z(0, z)$-field amplitude $B_z(0, 0)$ is fitted with Eq. 3.12. A current of $I = 5.0$ A results in magnetic field amplitude of $B_z(0, 0) \equiv \mu_0 I/(2R) = 9.5 \pm 0.7$ mT, while the expected value is $B_z(0, 0) = 10.4$ mT. The measured value differs slightly from the expected value, but is still within 10 %. This deviation is probably due to the fact that the lens has a finite length (50 mm), while Eq. 3.12 assumes an inifitely thin current loop.

From the model in Section 3.1, together with the position of the solenoid lens and the length of the setup it can now be estimated that the minimal resolvable temperature is around 1 K. This is estimated by demanding that the smallest obtainable spot size for $T = 1$ K still is larger than the resolution of 95 μm mentioned in Section 2.3 and that same spot is at least the same resolution larger for $T = 2$ K. From Eq. 3.8 can be seen that the spot size increases with $\sqrt{T}$, which means the difference in spot size becomes smaller for higher T. This will translate into a higher absolute uncertainty in temperature in the measurements with higher temperatures.

3.4 Data Analysis in Matlab

The analysis of the experiments described in Chapter 4 starts with recorded images from a CCD camera and time signals from an oscilloscope. The electrons that hit an MCP are multiplied and hit a phosphor screen where light is emitted. The light is imaged on the CCD camera with a positive lens. The current flowing from the MCP is recorded in time with the oscilloscope, which gives a measure for the total charge per electron bunch. The ionization laser intensity is measured by a photodiode and recorded in time on the oscilloscope. The difference in time between the ionization laser pulse and the bunch charge gives the time-of-flight (TOF) of the electrons.

The analysis of the measured data is primarily done in the Matlab programming environment from The Mathworks. A part consists of determining the transverse sizes of electron bunches from the CCD camera images. Another part consists of calculating the TOF from the laser pulse and bunch charge time signals recorded on the oscilloscope.

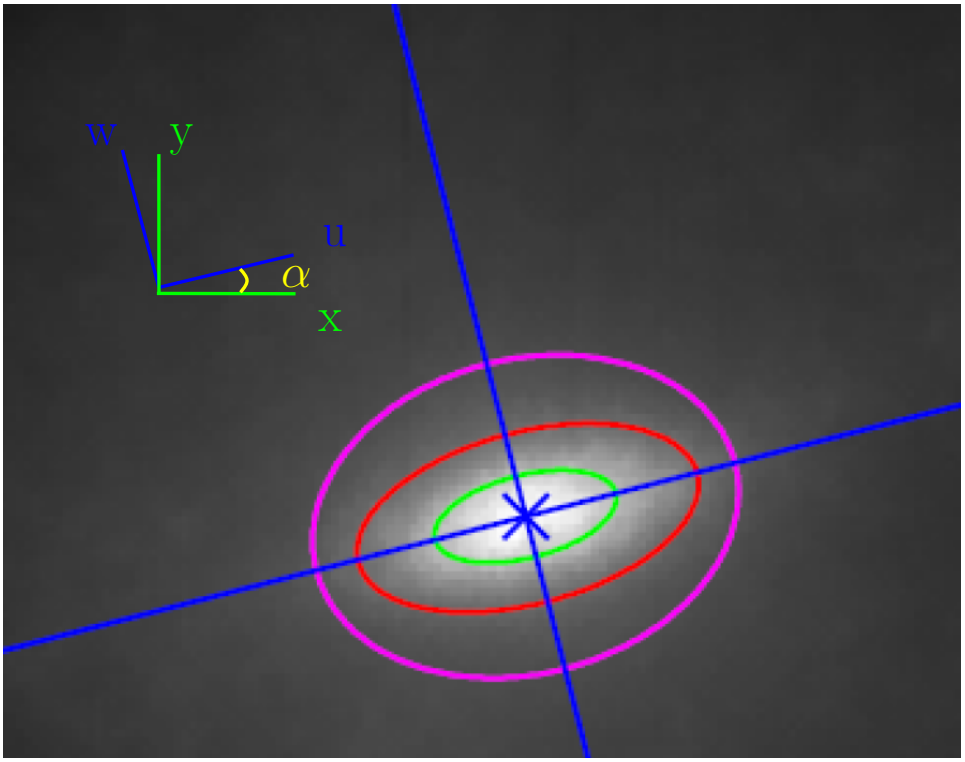

Figure 3.8 Part of a CCD camera image with an electron spot. The red line represents the trial ellipse fit. The blue cross is the center of the final fit, the blue lines are the axes u and w and the green and pink ellipses are the rms sizes from the top and bottom Gaussians, respectively.

3.4.1 CCD Image Analysis

The CCD images are analyzed with Matlab fitting routines, illustrated in Figure 3.8. In the figure part of a CCD camera image is visible, with an electron spot in the center. The image shows intensity in both x and y directions. The elongation of the (initially transverse round) electron bunch is due to the quadrupole in the setup, see Section 3.2. The orientation of the long axis of this ellipse is not the same as the symmetry axes of the quadrupole (assumed to be x and y), because the magnetic solenoid lens rotates the bunch under an angle α, as described by Eq. 3.13. Therefore, the relevant axes are the rotated axes u and w, which can transformed from x and y coordinates by:

$$u = x\,\cos(\alpha) + y\,\sin(\alpha) \qquad w = -x\,\sin(\alpha) + y\,\cos(\alpha). \tag{3.15}$$

The ellipses drawn in the figure are used in the explanation of the fitting routine below.

Figure 3.9 shows the spatial distribution of electrons along the w-axis. A combination of two Gaussian functions is used to correctly fit the data (blue

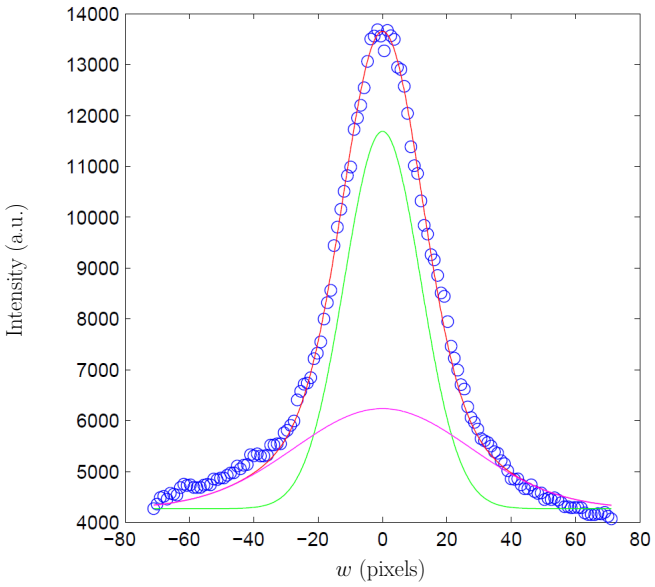

Figure 3.9 Fit of the intensity profile in Figure 3.8 of the u-axis. The blue circles are the data points. The green solid line is the top Gaussian, the pink solid line the bottom Gaussian and the red solid line the combined fit.

circles). This double Gaussian (red solid line) consists of a top Gaussian (green solid line) and a bottom Gaussian (pink solid line) that are added up. A single Gaussian does not fit well, because then the 'wings' of the fit drop off to steep. The spatial distribution of electrons has a similar shape in the u-direction, so the total function used for fitting is a 2D double Gaussian.

An analysis of both top and bottom Gaussians has been done. It showed that the rms spot sizes calculated from the top compare much better to GPT simulations than that from the bottom. In the analysis in Chapter 4, only the information of the top Gaussian is used for calculation of a temperature. The top part amounts for about 72 ± 11 % of the total number of particles in the bunches. The ratio between the top and bottom rms spot sizes is 0.4 ± 0.2. These numbers have been determined from a large dataset and the influence of specific parameters on the values has not been studied yet.

The reason for the double peak structure is not understood. For example, it cannot be a background signal in the detection system, because the electron bunches fall on different parts of the MCP, phosphor screen, lens and CCD camera, and the bottom Gaussian is always present.

The bottom Gaussian could come from a second signal of electrons reaching the detector from a different part of the MOT. However this would require the two lasers to intersect at another place in the MOT. A reflection of the ionization beam could explain that, but this is unlikely, because of the high precision of alignment that is needed to intersect the lasers in the first

place. Also, because the second spot is always present at the same relative location on the detector, it is unlikely that the lasers are the cause. They are re-aligned constantly in between experiments, and this would likely change the positions of the reflections.

Another possibility is that the MCP or other electronic system distorts the shape of the electron bunches. For now, the top Gaussian is considered to be the actual signal with the bottom Gaussian a distortion, either of physical origin (actual electrons that are created somewhere else) or due to the measurement system (MCP or other electronics).

The fitting routine first determines the center of the spot on the recorded CCD image, e.g. the point where the row and column with highest integrated intensity cross. It then determines in a few directions at which point the intensity has dropped 80 % with respect to the center point. On these points, an ellipse is drawn around the center point, which is the red ellipse in Figure 3.8. From this ellipse, the starting parameters for the actual fit are determined. The angle α is determined as the angle the long axis of the ellipse makes with the horizontal axis in the figure. This means $-\pi/2 \leq \alpha \leq \pi/2$ by definition. Two other parameters are the boundaries of the ellipse at both axes, which are an indication for the rms width of the bunch, and the intensity of the center point, which is a measure for the amplitude of the bunch intensity.

The final step is fitting the intensity of the CCD camera pictures with a double 2D Gaussian function:

$$G_2^d(u,w) = B + \frac{A_t}{2\pi\sigma_u^t\sigma_w^t}\exp\left[-\frac{1}{2}\left[\left(\frac{u}{\sigma_u^t}\right)^2 + \left(\frac{w}{\sigma_w^t}\right)^2\right]\right] + \frac{A_b}{2\pi\sigma_u^b\sigma_w^b}\exp\left[-\frac{1}{2}\left[\left(\frac{u}{\sigma_u^b}\right)^2 + \left(\frac{w}{\sigma_w^b}\right)^2\right]\right]. \tag{3.16}$$

Here, the σs are the rms sizes of the fit. Superscripts t and b represent the top and bottom Gaussian, respectively. Subscripts u and w represent the rotated axes. The angle α is also a fit parameter in Eq. 3.16. Background B is a constant and the As are the amplitudes of the Gaussians. In Figure 3.8, the blue cross indicates the center of the final fit, the blue lines represent the axes u and w and the green and pink ellipses show the rms sizes of the top and bottom Gaussians, respectively.

The top rms spot sizes are used in the final analysis of the temperature, described in Section 3.5.

3.4.2 Oscilloscope Analysis

In figures 3.10a and 3.10b, the ionization laser intensity on the photodiode and MCP current signals measured in time on a oscilloscope are fitted respectively. From the combination of the two, the TOF of electrons can

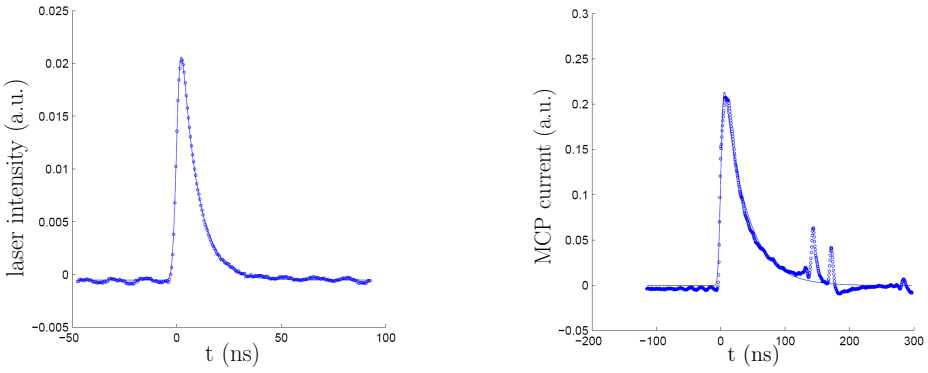

(a) **(b)**

Figure 3.10 Fits with Eq. 3.19 (solid line) of σ_g, τ_h and t_0 of time-signal measurements (dots) of (a) ionization laser intensity and (b) MCP current (b).

be determined. The original signals are both considered to be single 1D Gaussian functions:

$$G_1^s(t) = B + \frac{A}{\sqrt{2\pi}\sigma_g}\exp\left[-\frac{1}{2}\left(\frac{t}{\sigma_g}\right)^2\right], \tag{3.17}$$

where t is time and σ_g the corresponding rms value. The Gaussian is centered around $t = 0$ for mathematical convenience.

For both the photodiode and the MCP, a capacitance C and resistance R are between them and the oscilloscope. This means the signal gains an additional RC-time τ_h from the system from a transfer function:

$$H(t) = \frac{1}{\tau_h}\exp\left[-\frac{t}{\tau_h}\right]. \tag{3.18}$$

To fit the final signal S correctly, a convolution of G_1^s and H needs to be taken:

$$\begin{aligned} S(t) &= \int_{\infty}^{\infty} d\tau G_1^s(\tau) H(t-\tau) \\ &= \Omega\exp\left[-\frac{\tau_h t - \sigma_g^2/2}{\tau_h^2}\right], \end{aligned} \tag{3.19}$$

where Ω is:

$$\Omega = \frac{A\sigma_g}{\tau_h}\sqrt{\frac{\pi}{2}}\left[1 - \mathrm{erf}\left(-\sqrt{\frac{1}{2}}\frac{\tau_h t - \sigma_g^2}{\sigma_g \tau_h}\right)\right], \tag{3.20}$$

with erf(x) the error function of x.

For both the MCP current and the laser intensity, σ_g and τ_h are fitted. Also, in Eq. 3.19 the substitution $t = t - t_0$ has to be made, where t_0 is the offset in time for the maximum of the signal from the defined $t = 0$ on the oscilloscope. This t_0 is also a fit parameter which is used in TOF calculations that follow below.

The fits from figures 3.10a and 3.10b agree well with the data, except for some spikes in the MCP current figure, which are probably due to reflections in the cable connecting the detector to the oscilloscope.

In experiments, the spatial position of the center of the MOT can differ slightly from the defined origin in the chosen coordinate system. For the x and y directions this is not important: as long as the electron bunch travels through the beam line at a distance not too far from the z-axis, all the lenses will work the same as on-axis and this will only give small deviations from the simulations. The z-axis position of the center does matter, because that determines the place of the ionization volume in the accelerator structure and thus the longitudinal kinetic energy $U = p_z^2/(2m_e)$ of the electron bunch.

To include this z-position of the ionization volume in further analysis, the t_0 of the ionization laser pulse and the MCP current fits were used. The delay τ_d between the two signals relates to the TOF t_{tot} of the electrons from MOT to detector over a distance d_{tot}. This delay can be expressed as t_{tot} and an offset time τ_0 from the electronics:

$$\tau_d = t_{tot} + \tau_0 = d_{tot}\sqrt{\frac{m_e}{2fU}} + \tau_0, \tag{3.21}$$

where f is an additional fit-factor for the energy.

In Figure 3.11 a measurement is shown of the delay for different electron energies. The energy represents the energy of the bunch if it would come exactly from $z = 0$ m and follows from the applied acceleration voltage. The factor f in the fit effectively compensates for a small deviation in the z-direction. In this measurement, $f = 1.02 \pm 0.03$ and $\tau_0 = 19 \pm 1$ ns, which indicates that the electrons started almost from the center. For transverse temperature data analysis described in Section 3.5, the z-axis deviation in the simulations was determined using Eq. 3.21 and filling in the obtained delay times.

3.5 GPT Simulations

Fitted image data with the methods described in Section 3.4 is further analyzed with the model from Section 3.1 using simulation from General Particle Tracer (GPT), a simulation environment developed by Pulsar. GPT is software that simulates the trajectories of a set of charged particles with respect to defined magnetic and electric fields. Also, space charge forces can be taken into account.

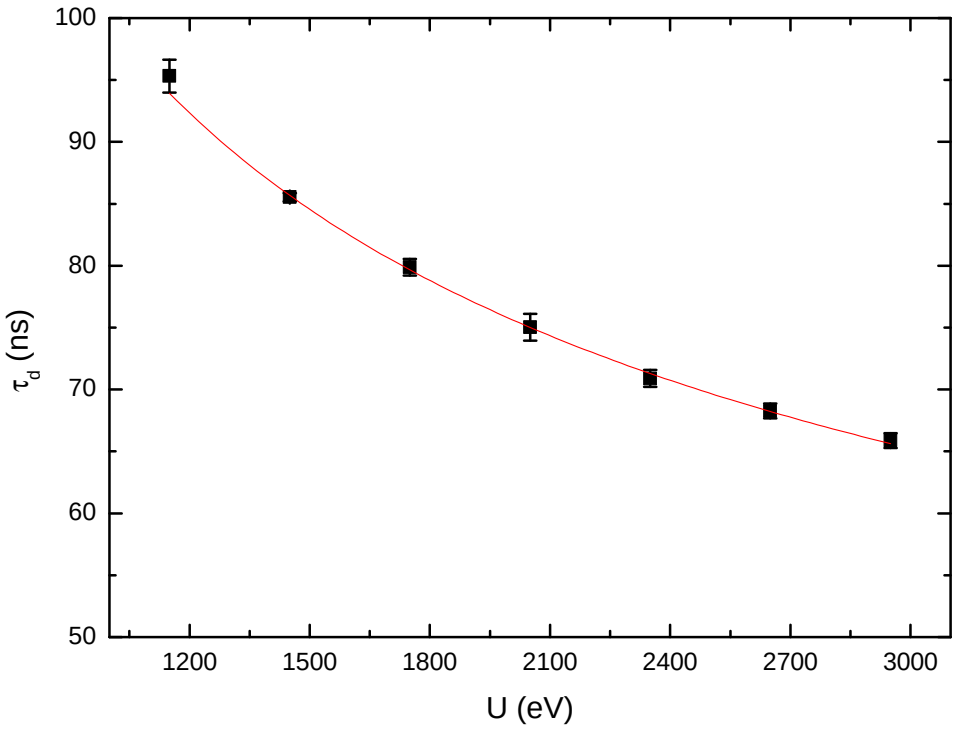

Figure 3.11 Delay τ_d between the laser ionization pulse signal and the MCP current signal as a function of electron energy U (black dots). The red line is a fit of the data with Eq. 3.21, with $f = 1.02 \pm 0.03$ and $\tau_0 = 19 \pm 1$ ns.

Compared to the optical model from Section 3.1, a more exact representation of the system can be obtained by putting electric and magnetic components in the simulations. For example, current loops are included that represent the MOT coils. The magnetic fields are calculated from this by the software and result in more accurate trajectories. This also holds for the other magnetic lenses, both the solenoid and the quadrupole. By using known parameters like current through the windings, radii, etc., the whole beam line is simulated. Also, the acceleration field map around the MOT has been calculated before [17] and is used in the simulations.

3.5.1 Fitting Procedure

GPT basically determines the position and momentum of particles at multiple positions or times in the beam line. Using enough particles that are distributed in the right way at the start of the beam line, statistically correct quantities like rms values of position and momentum distributions can be determined at any place or time in the beam line. In this case, the quantities of interest are calculated at $d = 1.53$ m, the position of the detector in the experiments.

The initial spatial distribution of electrons is determined by the excitation and ionization laser profiles, described in Section 2.2. For each simulation, the initial bunch sizes are put in. The initial momentum distribution is chosen equal in all three directions and can be expressed in terms of temperature. For a single direction, recalling Eq. 1.3 gives $\sigma_{p_{xi}} = \sqrt{m_e k_B T}$. The momentum distribution is Gaussian all three directions, representing a Maxwell-Boltzmann momentum distribution of electrons.

The final goal in the analysis here is to obtain a temperature from the data, using the information from the fitted spots from Section 3.4 and comparing them with GPT simulations. To accurately do that, scripts have been written in GPT to give as output the rms spot sizes in both directions in the rotated u-w frame. Both the rotation and elongation of the electron spot occur in the simulations as well. The rotation in the simulations is defined exactly the same way as in the fitted data, in order to compare the right quantities with each other. This has been extensively tested before fitting the actual data.

The GPT simulated spot sizes are corrected for the MCP resolution by quadratically adding up the simulated sizes and the resolution size. This way, the MCP resolution is also introduced in the simulations so they can more accurately be compared to the data. The effect is most important for small spot sizes near the resolution.

The last step in analysis is fitting the obtained spot sizes σ_u and σ_w from the CCD camera images to the corresponding ones in GPT. This is done by comparing data and simulation spot sizes as a function of current through the solenoid. A Matlab fitting script calls GPT with temperature

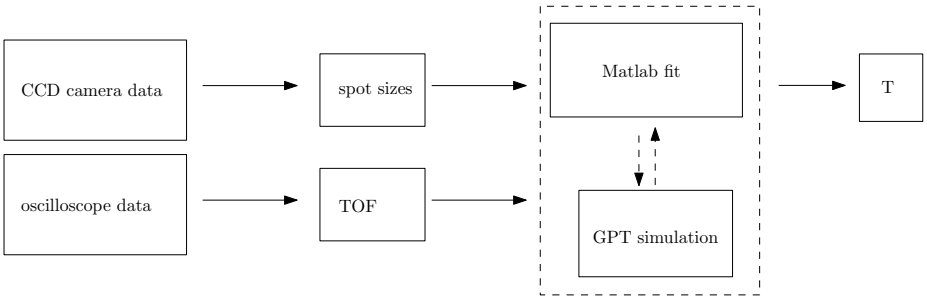

Figure 3.12 The analysis procedure from measured data to a final fitted temperature.

as a fitting parameter. GPT gives a simulation output, which is compared in Matlab with the data points. An error is determined for the fit. The temperature is then optimized for the smallest error, and an uncertainty in temperature is determined. This way, several of these waist scans (spot size vs. solenoid lens current) can be analyzed in a row, making it possible to analyze a lot of data in a relatively short amount of time. In Figure 3.12, the whole analysis procedure from beginning to end is illustrated.

3.5.2 Temperature and Its Uncertainty

In figures 3.13 and 3.14, a temperature fit and its error behaviour are shown, respectively. The temperature fit shows how well the simulation describes the experimental setup, seeing that both directions of the spot can be fitted simultaneously to a reasonable precision. Results shown in Chapter 4 are directly derived from these fitting routines.

The error χ^2 is used for the optimization routine in the fit, and is for both directions combined:

$$\chi^2 = \frac{\sum_{k=u,w}\sum_{j=1}^{N}(\sigma_{k,d_j} - \sigma_{k,s_j})^2}{2N}, \tag{3.22}$$

where σ_{k,d_j} is a spot size from the data, σ_{k,s_j} is the corresponding spot size from the simulation and N is the amount of points in the measurement series. The error is basically the added up (subscript j) quadratic difference between the data and simulation points, normalized to the amount of points. The errors of both u and w are included (subscript k) and the combined error is minimized in the simulations. For small linear changes in the fit parameter T, the error behaviour is quadratic with T, what can also be seen in Figure 3.14.

From the fitting procedure, 95 % confidence intervals are determined of the fit that are shown with the temperatures in Chapter 4. Another point of interest is the dependence of the fitting procedure on the parameters that are

fixed, for example the acceleration voltage, the initial position of the electron bunch, the focal lengths of the various lenses and the initial size of the bunch. A stability analysis of some of these parameters has been performed to check if the temperature fit can be trusted. Small changes of 10% in these parameters gave similar or smaller relative changes in temperature. This means the GPT simulations do not suffer from great instabilities in the total parameter space of the experiments. The temperature fit can therefore be trusted within an uncertainty that is comparable to that of the parameters. For most parameters like the acceleration voltage this is $\leq 1\%$, but the initial bunch sizes are known only within 10%.

The initial electron bunch sizes are determined by CCD cameras that measure the laser spot sizes. Measurements with ions have been done to verify this method. Ions only feel the initial (negative) exit kick lens effect, so from their final spot sizes the initial sizes of the ionization volume can quite accurately be determined, using $\sigma_f/\sigma_i = f_1/d_{tot}$. Here, the right side represents the magnification factor of the spot on the detector, being the focal distance f_1 divided by the total length of the setup d_{tot}. The CCD camera and ion bunch measurements agree with each other within 10%. Future measurements could include multiple ion bunch images to determine the spot size more accurately.

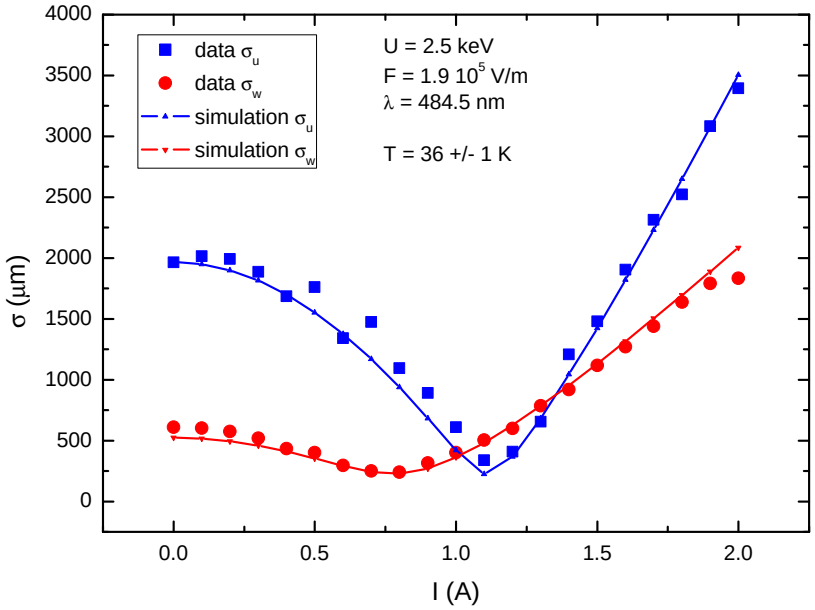

Figure 3.13 A fit with GPT of the spot sizes σ_u (blue) and σ_w (red) as a function of lens current with T as the fitting parameter. Data points are the circles and simulation points the squares with the line drawn through them. This figure is the final result of the fit.

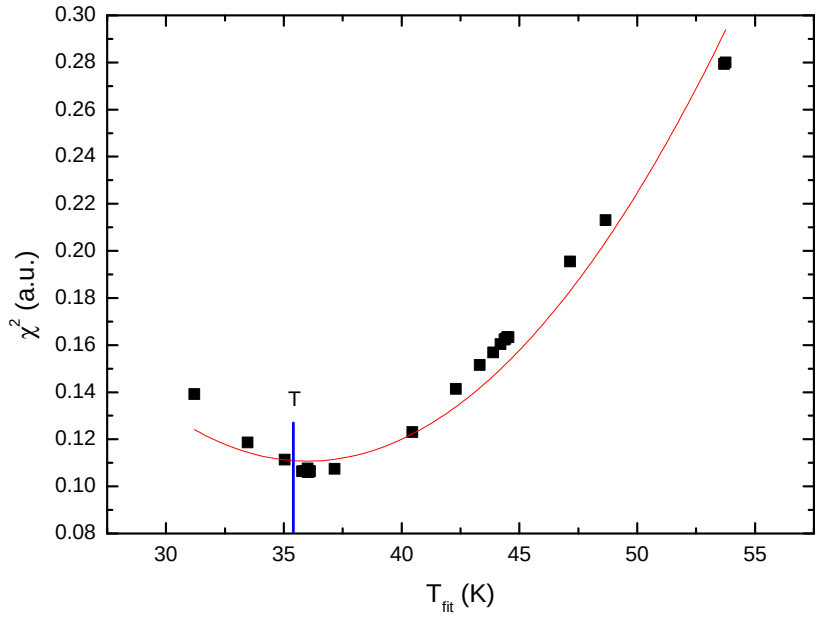

Figure 3.14 Error χ^2 of the GPT fit from Figure 3.13 as a function of temperature (black dots). This error is fitted with an parabola (red solid line) to show its quadratic behaviour. The final temperature acquired is indicated by the blue vertical line.

Chapter 4

Electron Source Temperature Measurements

In this chapter, measurements of the electron source temperature are presented. A distinction between two ionization processes is made, as described in Section 2.2. Photoionization of electrons in a DC electric field is discussed in Section 4.1. Rydberg atoms that are field-ionized in a pulsed electric field are the subject of Section 4.2.

4.1 Photoionization Measurements in a DC Electric Field

In Chapter 1, the UCP source is introduced, a new type of source that can create electron bunches with a low temperature. In this section, the lowest possible transverse temperature T is investigated, as well as the behaviour of T with excess energy E_{exc} of the electrons. Experiments were done using photoionization of electrons in a DC electric field. This combination allows the best measurements of T, because space charge forces between the electrons play no role.

To find T, the transverse final rms spot sizes σ_{x_f} of electron bunches are determined. They follow from CCD camera images of electrons incident on a MCP and phosphor screen detector. For a range of focal lengths of the magnetic solenoid lens, the spot sizes are compared to those of GPT simulations. These simulations describe the electron trajectories in the setup in detail, see Section 3.5. The temperature is included in the simulations by relating it to the initial rms momentum of the electrons, from Eq. 1.3, $\sigma_{p_{xi}} = \sqrt{m_e k_b T}$. An iterative fitting procedure using GPT results in a T that fits the data best.

In Chapter 2, the electron excess energy is introduced, Eq. 2.8:

$$E_{exc} = E_\lambda + E_{Stark} = hc\left(\frac{1}{\lambda} - \frac{1}{\lambda_0}\right) + 4Ry\sqrt{\frac{\mathcal{F}}{\mathcal{F}_0}}.$$

The field-dependent term containing the electric field strength $\mathcal{F}$ influences the ionization threshold of Rb. If a fixed ionization laser wavelength λ is chosen, a higher $\mathcal{F}$ lowers the ionization threshold. More excess energy is then transferred to the electrons in the ionization process. The goal of the experiments is to investigate how the transverse temperature depends on E_{exc}, either by varying λ or by varying $\mathcal{F}$.

A simple model for the ionized electrons is that all their excess energy is kinetic, with no preferential direction of momentum for the electrons:

$$\frac{3}{2}k_B T = E_{exc}. \tag{4.1}$$

In this model, each direction has the same temperature. Therefore, a general T can be derived from the two transverse spot size measurements, because their combined kinetic energy simply represents 2/3 of the total excess energy. It is referred to in this thesis as the 'linear model'.

4.1.1 Experimental Conditions

The initial spatial distribution of the electron bunches is determined by the excitation and ionization laser profiles, as mentioned in Section 2.2. These sizes are derived from CCD cameras that determine the laser spot sizes at the center of the MOT. In the experiments, the bunch sizes are $\sigma_{x_i} = 19 \pm 2$ μm, $\sigma_{y_i} = 25 \pm 3$ μm and $\sigma_{z_i} = 30 \pm 3$ μm.

However, the bunch size in the z-direction is actually much larger because of the laser pulse length. Over an rms time of $\sigma_t = 2.5$ ns, the ionization laser frees electrons. When ionized, the electrons are accelerated immediately, creating a bunch of the same temporal length as the laser pulse. This temporal length translates to a rms spatial length of $\sigma_z = 47$ mm for a beam of $U = 1$ keV. Compared to typical transverse lengths of $\sigma_\perp = 25$ μm, this is three orders of magnitude larger. This effect is not included in the GPT simulations. Because space charge forces are excluded in the simulations, it is irrelevant what σ_{zi} is, because it has no effect on the calculated sizes in both transverse directions.

An estimation of the potential energy U_p of an electron bunch of charge Q is made in ref. [24]. The calculation uses a homogeneous charge density distribution in an ellipsoidal bunch. The potential energy of a single electron in the bunch is:

$$U_q = \frac{3}{20}\frac{Qe}{\pi\epsilon_0\sigma_z}\frac{\arctan\,\Lambda}{\Lambda}, \tag{4.2}$$

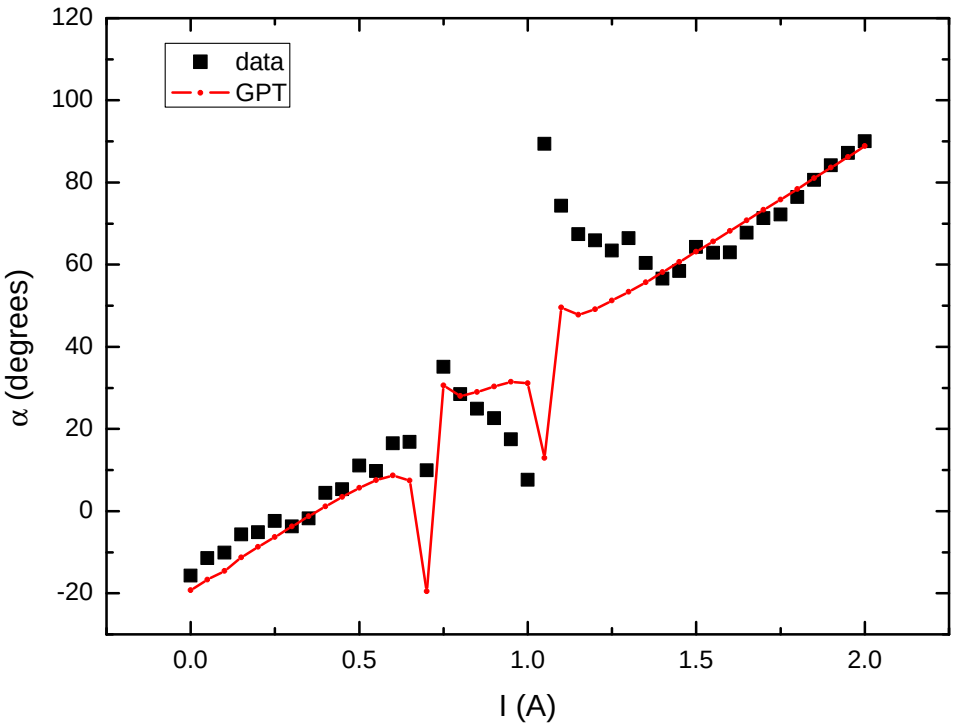

Figure 4.1 Angle α as a function lens current I where electron energy was $U = 1.5$ keV. Measurements (black squares) are compared with GPT simulations (red solid line). The simulated angle has an offset of $\alpha = 15\ ^o$.

where Λ is the eccentricity of the ellipsoid. The bunch is cylindrically symmetric, with z the axis of symmetry, leading to an Λ defined as:

$$\Lambda = \sqrt{1 - \frac{\sigma_x^2}{\sigma_z^2}}. \tag{4.3}$$

For the lengths and charge mentioned above, $\Lambda \simeq 1$, which results in $U_q = 0.090$ meV. Kinetic energy for a low temperature $T = 10$ K bunch is still $k_B T = 0.86$ meV, which is an order of magnitude larger. The space charge forces are therefore ignored in the analysis of the photoionization experiments.

In Chapter 3, the angle α was introduced to include the rotation in the analysis of the two transverse spot sizes of the bunch. A measurement has been performed of α as a function of magnetic solenoid lens current I to check its behaviour. Recalling Eq. 3.13, $\alpha \sim B_z(0, z) \sim I$, so a linear dependence on I is expected. For an electron energy $U = 1.5$ keV, the measured angle as a function of lens current is shown in Figure 4.1.

In the figure the expected linear behaviour is observed in the measurements. GPT simulations have been performed for comparison. The simu-

lations show the same slope of $d\alpha/dI = 55\ ^o$/A. An offset of $\alpha = 15\ ^o$ is needed to match the measurements. Initially, the bunch is oriented along the y-axis, meaning $\alpha = 90\ ^o$. If the magnetic solenoid lens is switched off, the total rotation is $\Delta\alpha = -110\ ^o$, giving $\alpha = -20\ ^o$. This is due to the MOT coils and the quadrupole. The offset is therefore only a small correction. It can be explained by small differences between the actual beam line and the simulations. Steering coils or other sources of small magnetic fields can add to the rotation of the bunch.

In the simulations and the data, two sharp deviations occur near $I = 0.8$ A and $I = 1.1$ A. These are the points where the two transverse spot sizes of the bunch are equal and the calculation of the angle becomes difficult. These points are also visible in the fit of the spot sizes shown in Figure 3.13, where they occur at $I = 1.0$ A and $I = 1.3$ A.

The agreement between data and simulation is an indication that the setup is characterized well.

4.1.2 Experimental Results

For different ionization wavelengths λ, the transverse temperature of electrons T has been determined. For a field strength of $\mathcal{F} = 1.85 \cdot 10^5$ V/m, the results are shown in Figure 4.2. The part of excess energy associated with the laser energy is $E_\lambda = -26$ - $+39$ meV. The negative energies still ionize the electrons, because of the extra energy from the Stark shift $E_{Stark} = 33$ meV for this field. This is also indicated in the figure.

In the figure, a dependence of transverse temperature on kinetic excess energy is apparent. Temperatures as low as $T = 16$ K have been measured for this field strength, close to the ionization threshold. At the shortest wavelengths, temperatures around $T = 500$ K are reached. Clearly, a higher E_{exc} increases T, but the data shows a nonlinear behaviour. This means that the fraction of excess energy that is put into the transverse directions is not constant over E_{exc}.

To vary the excess energy of electrons, also the acceleration field strength can be changed. For a range of field strengths $\mathcal{F} = (1.11 - 2.15) \cdot 10^5$ V/m ($E_{Stark} = 25$ - 35 meV), the initial transverse temperature of electrons is shown in Figure 4.3. The wavelength of the ionization laser was fixed at $\lambda = 478.0$ nm ($E_\lambda = 6$ meV) in these experiments. The linear model from Eq. 4.1 is also indicated in the figure.

The temperature follows the same trend as the model with varying field strength. The behaviour is linear, but the data has a different temperature offset compared to the model. The dotted line is drawn through the data points as a comparison to the model, with a slope $dT/dE_{exc} = 8.4$ K/meV.

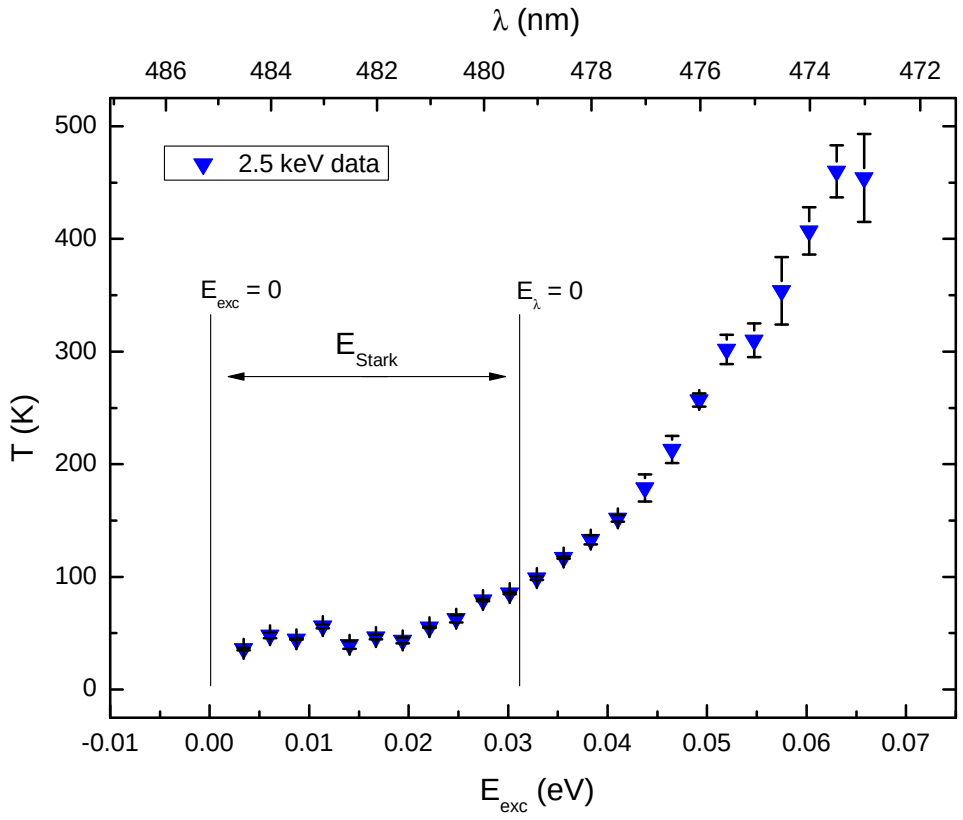

Figure 4.2 The initial transverse electron temperature as a function of excess energy. Indicated in the figure is the fixed Stark energy $E_{Stark} = 33$ meV, for $\mathcal{F} = 1.85 \times 10^5$ V/m. The ionization laser wavelength is varied over $\lambda = 473.0$ to 484.0 nm ($E_\lambda = -26$ - $+39$ meV) to obtain this excess energy range.

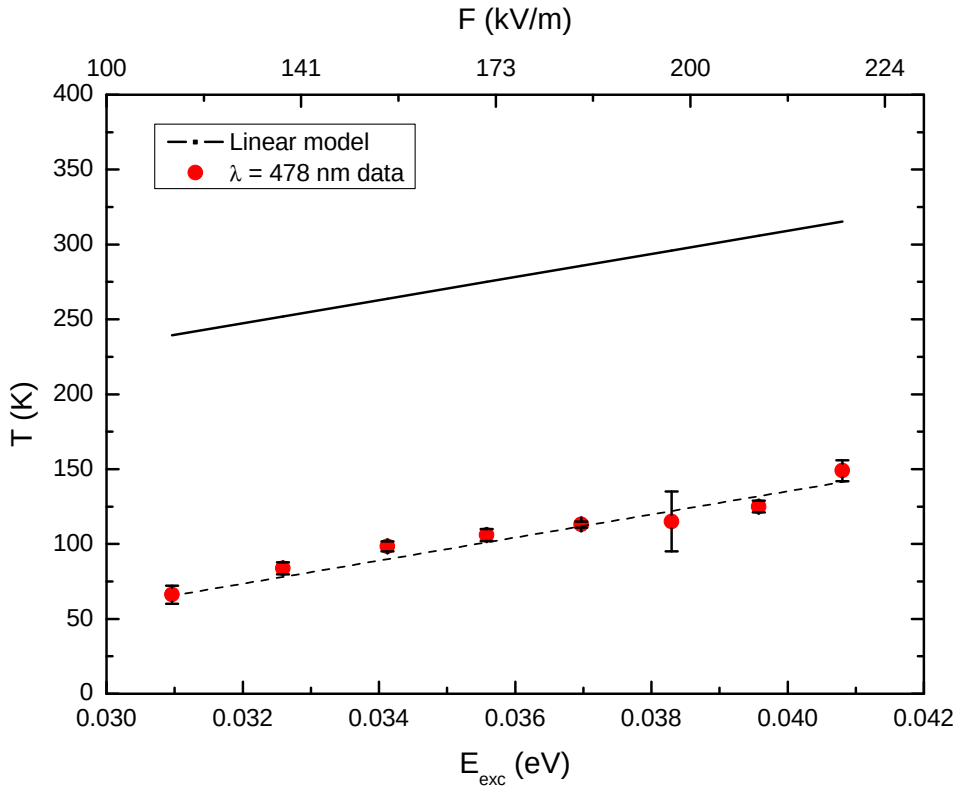

Figure 4.3 The initial transverse electron temperature as a function of excess energy. The electric field strength was varied to create the excess energy range over $\mathcal{F} = (1.11 - 2.15) \cdot 10^5$ V/m (E_{Stark} = 25 - 35 meV). The ionization laser wavelength was fixed at λ = 478 nm (E_λ = 6 meV). The expected temperature from Eq. 4.1 is indicated by the black line. The dotted line has the same slope and is drawn through the data points for comparison.

In Figure 4.4, T is shown as function of E_λ for varying wavelength. Now two different field strengths are shown, $\mathcal{F} = 1.11 \cdot 10^5$ V/m and $\mathcal{F} = 1.85 \cdot 10^5$ V/m, which is the same data set as in Figure 4.2. The wavelength range is $\lambda = 477.0 - 482.5$ nm. The field strength dependence already shown in Figure 4.3 seems to be constant over the whole wavelength range. This means that E_{exc} is a good energy scale to compare data on, because it incorporates both the ionization wavelength and field strength effects, as expected from Eq. 2.8.

In Figure 4.5, the same ionization laser wavelength scan of electron temperature is shown for three different field strengths $\mathcal{F}$, but now as a function of E_{exc} again. This figure basically combines the measurements from figures 4.2 and 4.3 for the entire dataset. An universal behaviour is observed for different Stark shifts. This is an indication that the measurement technique is quite robust and the data analysis can be trusted.

The data is also compared to the linear model from Eq. 4.1 in the figure. What can be seen is that the measured transverse temperature approaches the model for low excess energy. For higher excess energy the temperature becomes lower than expected, but at the highest energies it seems to approach the model again. Experiments at even higher field strengths would enable an extension of the energy range, which could bring more understanding of the ionization process high above the threshold. The accelerator structure allows field strengths up to $\mathcal{F} = 1.11 \cdot 10^6$ V/m corresponding to $V = 30$ kV.

The overall lowest temperature measured is $T = 10.7 \pm 0.8$ K. For this measurement, the initial spot sizes of the electron bunch were around $\sigma_i = 25$ μm. The minimum final spot sizes were around $\sigma_f = 100$ μm, which gives a transverse coherence length of $L_\perp = 36$. This is comparable to the coherence length of $L_\perp = 38$ nm that is mentioned in Chapter 1, which is good enough for single-shot UED of proteins. However, the bunch charge was around $Q = 1 - 10$ fC, the energy $U = 2.5$ keV and the pulse length $\sigma_t = 2.5$ns. This is not yet in the range of $Q = 100$ fC, $U = 100$ keV and $\sigma_t = 1$ ps needed for actual single-shot UED measurements of protein crystals.

For low E_{exc} really close to the ionization threshold, the bunch charge became too low to determine the spot sizes. Therefore, even lower temperatures could not be measured. One reason for this can be that close to, but still above the ionization threshold a quasi-continuum of energy states exists for the Rb atom [25]. An electron that is barely ionized is still influenced by the ion core. This can lead to ionization-photon absorption cross-sections that are small for certain photon energies, while being very high for other photon energies. This situation is comparable to that of Rydberg energy levels, just below ionization threshold, the subject of Section 4.2. What this exactly means for the bunch charge will have to be investigated further.

Other effects that might explain the low temperature limit are ion-electron interactions in the initial volume and lens aberrations in the beam

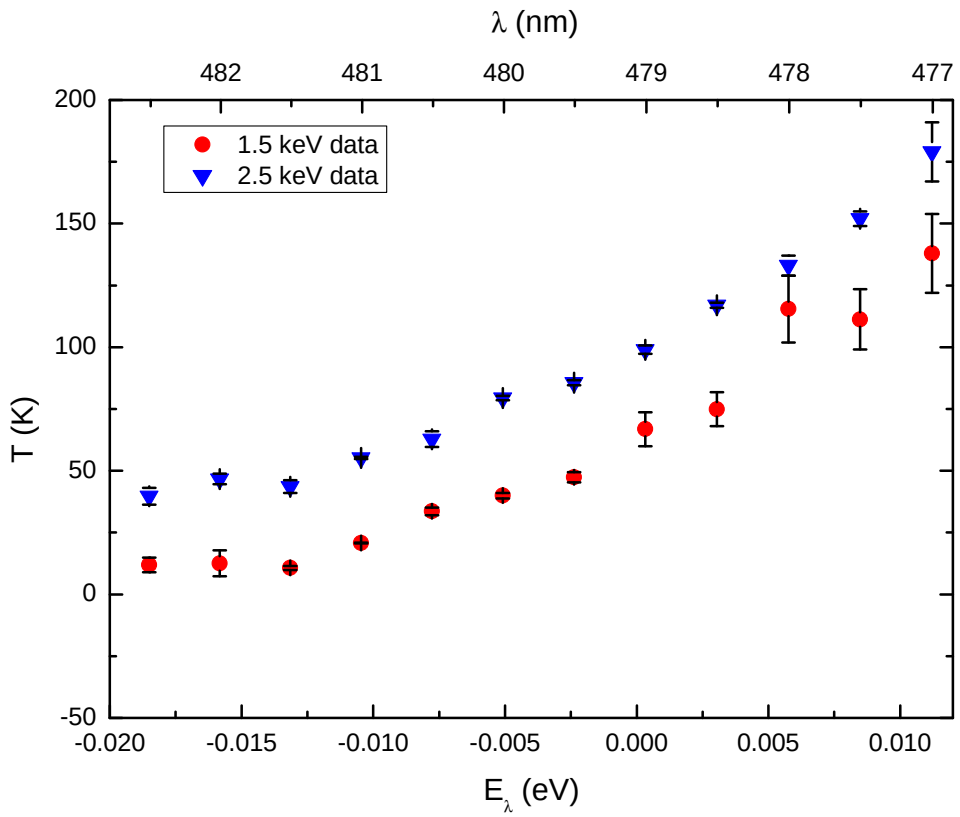

Figure 4.4 The initial transverse temperature of electrons as a function of photon energy E_λ. The data shown if for two different field strengths $\mathcal{F} = 1.11 \cdot 10^5$ V/m (red dots) and $\mathcal{F} = 1.85 \cdot 10^5$ V/m (blue inverse triangles)

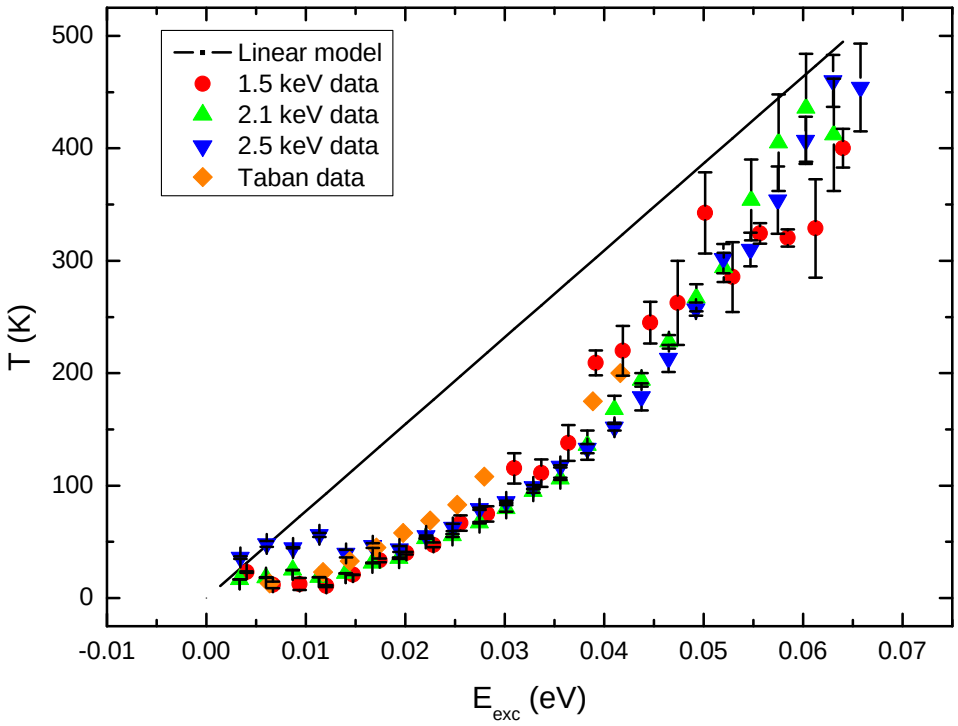

Figure 4.5 The initial transverse electron temperature as a function of excess energy. The ionization wavelength was varied to create the excess energy range. This was done for three different acceleration fields: $\mathcal{F} = 1.11 \cdot 10^5$ V/m (red dots), $\mathcal{F} = 1.55 \cdot 10^5$ V/m (green triangles) and $\mathcal{F} = 1.85 \cdot 10^5$ V/m (blue inverse triangles). The expected temperature from the linear model, Eq. 4.1, is indicated by the black line. Previously obtained data by Taban [4] is included for comparison (orange diamonds).

line, which both increase the spot sizes. This leads to a higher temperature derived from the final spot sizes. These effects are only important at low temperatures. In future experiments, more bunch charge could be used to also measure the temperature of the low excess energy regime ($E_{exc} \leq 0.10$ meV).

Another interesting feature visible in the figure is a small dependence on field strength at low energies. This little 'bumb' in temperature seems to become more apparent for higher field strengths, but is always located near the ionization threshold. More experiments can be done to investigate this behaviour.

A previously measured data set by Taban [4] is also included in the figure. In these measurements, the temperature was extracted from waist scans using the energy U as a scanning parameter, meaning also a varying field strength $\mathcal{F}$, resulting in an averaged T. The field strength was typically between $\mathcal{F} = (0.48 \text{ - } 1.11) \cdot 10^5$ V/m, corresponding to $E_{Stark} = 17 \text{ - } 25$ eV. From Figure 4.3 and the mentioned slope of $dT/dE_{exc} = 8.4$ K/meV, this means the difference between the maximum and minimum temperature in this range is around $\Delta T = 67$ K.

The Taban data follows the same trend as the experiments described here. This is remarkable, realizing that the data is obtained from an averaged temperature and the experiments are performed in a different setup. Although it compares quite well, the averaged old data shows no 'bump' near the ionization threshold and it seems to diverge slightly from the new data at higher energies.

4.1.3 Temperature Models

For the model from Eq. 4.1, it is assumed that the electron is ionized and the excess energy is transfered completely to the electron. The kinetic energy that it gains is equal in all three directions, which means that the momenta of the particles are distributed identically in x, y and z. In other words, the model represents that 1/3 of the excess energy equals the kinetic energy associated with one direction. It can be seen in the measurements that this is not true.

In Eq. 2.8, the excess energy in an electric field is expressed as the field-free excess energy with an added Stark shift. However, this is not the complete description of the system, because it does not include dynamics of the particles in time. An electron is created in Coulomb and Stark potentials. The initial momentum of an electron is influenced by the ionic Coulomb potential during its travel toward the detector. A different momentum distribution of electrons results in a different temperature, which makes it important to include this effect in the modelling of the temperature. The calculations of the electron trajectories in time can be done either classically [26] or quantum mechanically [25, 27].

In ref. [26], the potential for these classical electrons orbiting an ion core in an external electric field strength $\mathcal{F}$ is given:

$$V_{CS} = -\frac{e^2}{4\pi\epsilon_0\rho} - e\mathcal{F}z, \tag{4.4}$$

with ρ the distance of the electron to the core and $-z$ the direction of the electric field. This potential represents the Coulomb and Stark potentials combined.

The trajectory of an electron can be calculated analytically in parabolic coordinates, given an initial position on a sphere around the ion core and the excess energy E_{exc} of an electron. Parabolic coordinates ξ, η and ϕ can be expressed in Cartesian coordinates x, y and z [26, 27]:

$$\begin{aligned}
\xi &= \sqrt{\sqrt{x^2+y^2+z^2}+z}, \\
\eta &= \sqrt{\sqrt{x^2+y^2+z^2}-z}, \\
\phi &= \arctan\frac{y}{x}.
\end{aligned} \tag{4.5}$$

The calculations consist of solving the equations of motion in these coordinates, details can be found in ref. [26], but here the main aspects of this model are treated.

In this coordinate system, an electron in the potential from Eq. 4.4 can be described separately in the ξ and η coordinates. In the ξ direction, the electron performs a periodic motion around the ξ-axis in time. There can be several oscillations before the electron escapes the ion core.

In the η direction, the electron can be free or bound depending on the energy E_{exc}. There are three energy ranges that are of importance. If $E_{exc} \leq 0$, meaning an energy below the Stark-shifted ionization threshold, the electron is always bound. If $0 < E_{exc} \leq 4Ry\sqrt{\mathcal{F}/\mathcal{F}_0}$, meaning an energy between the Stark-shifted and field-free ionization threshold, the electron can escape above a critical angle β_c with the $-z$-axis [26]:

$$\beta_c = 2\ \arcsin\ (1 - \frac{E_{exc}}{4Ry\sqrt{\frac{\mathcal{F}}{\mathcal{F}_0}}}). \tag{4.6}$$

If $E_{exc} > 4Ry\sqrt{\mathcal{F}/\mathcal{F}_0}$, meaning an energy above the field-free ionization threshold, the electron can always escape.

In Figure 4.6, electron trajectories are shown for a simple potential consisting only of the acceleration field (solid lines) and that for the potential from Eq. 4.4 (dotted lines) [26]. The excess energy of electrons is really low in this example, $E_{exc} = 0.24$ meV, so the effect of the ion core is quite large. It is clear that this is an effect to account for when calculating the final momentum distribution.

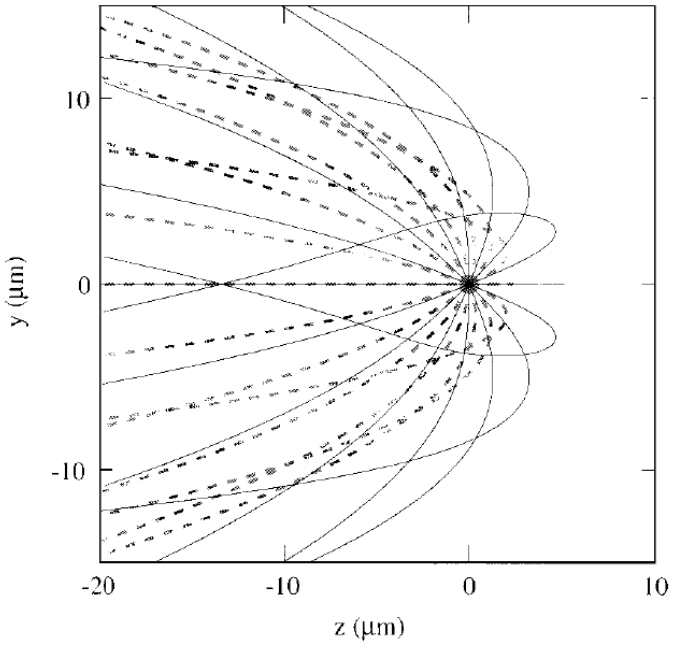

Figure 4.6 Electron trajectories for $E_{exc} = 0.24$ meV: simple ballistic calculations (dotted lines) and exact calculations including the Coulomb forces from the ion core (solid lines). From [26].

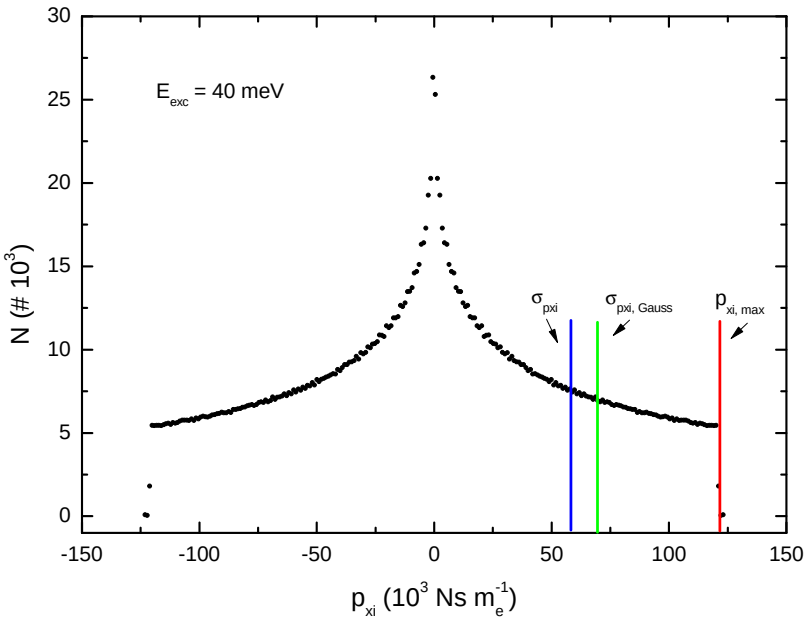

Figure 4.7 Histogram of p_{xi} of the classical trajectory model for $E_{exc} = 40$ meV. Indicated with the blue line is $\sigma_{p_{xi}}$, with the green line the rms momentum for a corresponding Gaussian distribution $\sigma_{p_{xi,\mathrm{Gauss}}}$ and with the red line the maximum momentum $p_{xi,\mathrm{max}}$.

The same model as in the article was used in Matlab simulations of the electron trajectories. The relevant parameters were chosen in the simulations so that they represent the measurements done in the UCP setup. A large number of electrons trajectories were simulated, using a uniform spatial initial distribution of electrons around their ion cores.

For $N = 10^6$ particles, the momenta of the particles in the transverse direction x were calculated at a position tens of μms away from the core, where the Coulomb potential no longer plays any role. The only important force that remains is the acceleration field in the longitudinal z direction, but this does not influence the transverse momenta of the electrons. The rms momentum is then translated into a transverse temperature, using the relation $\sigma_{p_{xi}} = \sqrt{m_e k_B T}$ from Eq. 1.3.

The momentum distribution p_{xi} for $E_{exc} = 40$ meV is shown in Figure 4.7 in the form of a histogram. Indicated is the rms value $\sigma_{p_{xi}}$. It is clear this distribution is not Gaussian, for which the corresponding rms momentum has also been included in the figure. Compared to a Gaussian distribution, there are more electrons with low transverse velocity, leading to a lower $\sigma_{p_{xi}}$. This corresponds to a lower temperature, which is also visible in the measurements. As a check for the model, the maximum momentum from the ionization process is indicated in the figure, which corresponds to a sharp drop to zero particles in the histogram.

A third model for the transverse temperature follows from quantum mechanical calculations performed by Vredenbregt and Sanders [25]. The model calculates the solutions to the Schrödinger equation in parabolic coordinates using the potential from Eq. 4.4. Then, at a large distance from the ion core, the momentum operator is used to calculate the rms wave numbers in the transverse x-direction of the electron. This is finally translated into a temperature, analogous to the classical calculations.

4.1.4 Model Comparison

In Figure 4.8, the classical and quantum mechanical trajectory models are compared to the linear model from Eq. 4.1 in a temperature versus excess energy plot. The $\mathcal{F} = 1.85 \cdot 10^5$ V/m dataset is also included. All models predict a different behaviour and none of them matches the data perfectly. The classical model is calculated with a field strength of $\mathcal{F} = 1.11 \cdot 10^5$ V/m and the quantum mechanical calculations were performed with a field strength of $\mathcal{F} = 0.76 \cdot 10^5$ V/m.

However, what is clear from the classical and quantum mechanical calculations, is that a different transverse temperature behaviour is expected. Clearly, the Coulomb and Stark potential combined result in a lower rms momentum in the two transverse directions x and y. This can be seen in the figure that shows the transverse temperature. The two trajectory models both predict a lower transverse temperature behaviour than the linear

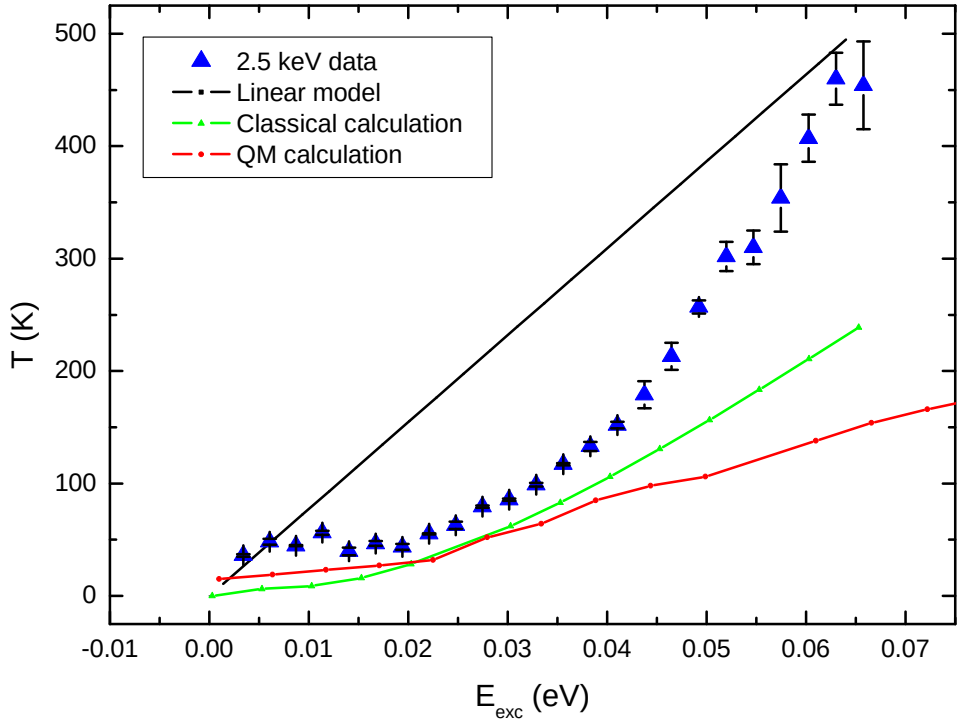

Figure 4.8 The initial transverse temperature of electrons as a function of excess energy. The linear model and the classical ($\mathcal{F} = 1.11 \cdot 10^5$ V/m) and quantum mechanical ($\mathcal{F} = 0.76 \cdot 10^5$ V/m) trajectory models are compared to data ($\mathcal{F} = 1.85 \cdot 10^5$ V/m).

model. This observation agrees with the data, although not quantitatively. Especially for higher energies, the models seem to diverge from the data and from each other.

In the classical model, the initial spatial distribution of electrons with respect to the ion core is not included correctly. The electrons are assumed to be uniformly distributed on a sphere around the ion core, but this is not true in an electric field pointing in one direction. Including the right distribution might result in a better agreement between the data and the model.

In the quantum mechanical model, the solutions to the Schrödinger equation are calculated. A single temperature is then calculated by averaging over the different solutions. However, the appropriate weight factors for the different solutions have not yet been included yet [25], which could change the transverse temperature behaviour.

Another addition to both models can be a more realistic Coulomb potential. Now the models use a potential of a Hydrogen atom with a positively charged point source in the center. The screening effect of other electrons shells in Rb can be included to modify the simple $1/r$ potential. This might reduce the effect of the ionic core at higher energies and result in a more accurate description of the data.

4.2 Field-Ionization Measurements with Rydberg Atoms

Experiments described in this section were done with Rydberg atoms ionized by a pulsed electric field. This process should result in electron bunches with rms temporal lengths in the order of $\sigma_t = 50$ ps [4], creating bunches more suitable for UED compared to those made with photoionization.

4.2.1 Experimental Conditions

To field-ionize Rb atoms, the outer electron must orbit the atom very far from the core, so that they can be pulled away by the electric field when it is switched on. The Stark shift is $E_{Stark} = 18$ meV for a typical field of $\mathcal{F} = 5.55{\cdot}10^4$ V/m, corresponding to an acceleration voltage of $V = 1.50$ kV. Energy levels of electrons that are just below the ionization threshold with a binding energy that is smaller than the Stark shift can be ionized. The Stark shift is in the range of Rydberg energy levels, introduced in Section 2.2. In the experiments described here, Rydberg states $n = 35 - 28$ were used with angular momentum quantum number $L = 0$ (the S-states). This corresponds to Stark shifts needed for ionization of $E_{Stark} = 15 - 23$ meV. Electron bunch sizes used in the experiments are $\sigma_{x_i} = 35{\pm}4$ μm, $\sigma_{y_i} = 50{\pm}5$ μm and $\sigma_{z_i} = 50 \pm 5$ μm.

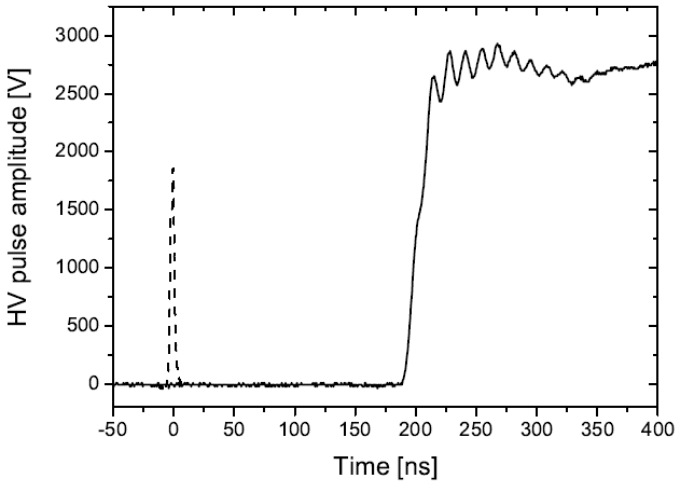

Figure 4.9 High voltage (3 kV) electric field pulse measurement in time (solid line). The excitation laser signal used for creating Rydberg atoms is also indicated (dotted line). From [4].

These field-ionization measurements were done before the setup was changed to that described in Chapter 3. A shorter beam line of total length $d_{tot} = 0.65$ m was used, compared to the $d_{tot} = 1.53$ m in the DC photoionization experiments. Also, the magnetic solenoid lens was not present. Therefore, waist scans using the lens as a scanning parameter were not possible. Instead, the bunch sizes were measured for different Rydberg states n, which effectively means that the electron energy U was varied.

The CCD images were analyzed with a single 2D Gaussian fit function. This means the agreement with the data is not as good as in the DC photoionization experiments where the double 2D Gaussian fit functions were used. However, completely new data structures and analysis scripts prevented the re-analysis of the old data. Compared to the double 2D Gaussian fit procedure, the rms spot sizes are overestimated, which results in the final analysis in an overestimation of the temperature.

As an example, for the Rydberg $n = 28$ state, the ionization laser wavelength is set to $\lambda = 483.16$ nm. The electric field is switched on from $V = 0$ to 3 kV with a typical rise-time of $\tau_{acc} = 17$ ns. The high voltage pulse signal in time is shown in Figure 4.9 [4]. About 200 ns after excitation, the voltage is switched on. At a voltage of $V = 2512$ V ($U = 1256$ eV), the electrons are ionized and accelerated. For higher n, the point of acceleration is lower in voltage, because these states are closer to the field-free ionization threshold.

4.2.2 Experimental Results

For each Rydberg state, 100 single-shot measurements were performed. For each shot, a CCD image was recorded and transverse bunch sizes were determined. The area $2\pi\sigma_u\sigma_w$ of the intensity profile was used to calculate the charge Q with the charge calibration of the detector, see Section 2.3.

The bunch size of the electrons in the z-direction was now completely determined by the excitation laser intensity profile. The electrons were excited and collectively ionized by the electric field. This is different from the DC photoionization experiments, Section 4.1, where the ionization laser pulse length determined σ_{z_i}. Because the bunch length in the z-direction for these bunches now was much smaller than in the DC photoionization experiments, space charge effects started to play a role. The average potential energy of an electron in the bunch increases linearly with Q. This adds an effective extra kinetic energy $\sigma_{p_q}^2/(2m_e)$ to the electron bunch, where σ_{p_q} is the added rms momentum due to charge [4].

If the initial size term from Eq. 3.8 is small, the final bunch size σ_{x_f} is mostly determined by the rms momentum of the bunch. It can be expected that the spot size then increases with $\sqrt{Q}$. In Figure 4.10, the squared rms spot size in the rotated u-direction (long axis of the electron bunch) is plotted as a function of charge. A linear fit of σ_{x_i} with $\sqrt{Q}$ shows an agreement with the prediction. The fit is performed over the half of the points with the highest charge, because the lower charge measurements have a lower precision in the analysis of their CCD images. The figure shows the points of Rydberg state $n = 34$. The charge data is extrapolated to $Q = 0$ to obtain electron bunch sizes without space charge effects.

For all 8 measured Rydberg states, both zero-charge rms spot sizes have been analyzed, illustrated in Figure 4.11. The spot sizes σ_u and σ_w are shown as a function of acceleration energy U. Each energy represents a Rydberg state n. The data is analyzed with GPT simulations assuming a single T for all n.

It is not possible to characterize the data completely with the simulations. The simulations shown in the figure have the smallest error for the two transverse directions combined. The resulting temperature is about $T = 50$ K, which is an indication for the order of magnitude of the temperature the field-ionized electrons have.

The transverse temperature is calculated over a range of energies. It is not understood what the temperature of field-ionized electrons should be, nor what its dependence on energy is. The next experimental step could be to measure the temperature of a single Rydberg energy state with the method used for the DC photoionization experiments. The magnetic solenoid lens gives an independent way of determining the temperature, and therefore the temperature dependence on energy or other relevant parameters can be studied.

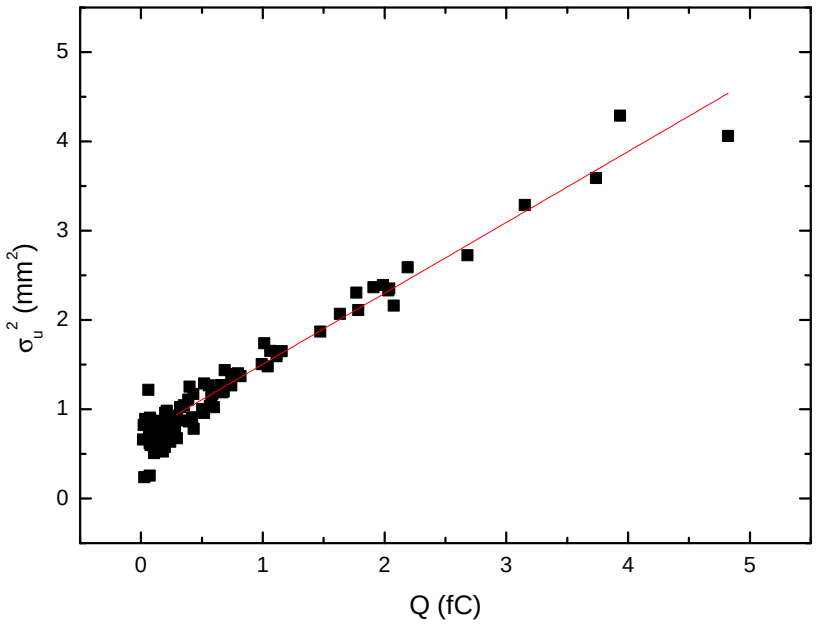

Figure 4.10 Squared spot size in the u-direction (long axis of the electron bunch) against bunch charge Q (black dots) for Rydberg state $n = 34$. The red line is a linear fit of σ_u^2 versus Q.

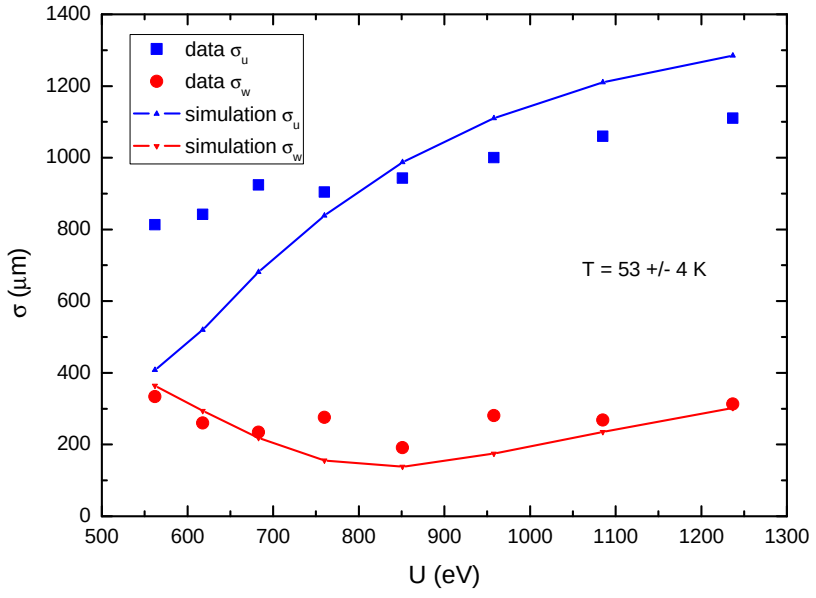

Figure 4.11 A fit with GPT of the rms spot sizes σ_u (blue) and σ_w (red) for $Q = 0$ as a function of electron energy U ($n = 35 - 28$ from left to right) with T as the fitting parameter. Data points are the circles and simulation points the squares with the line drawn through them. This figure is the final result of the fit.

Chapter 5

Conclusion

In this thesis, experiments are presented of the initial transverse temperature of electron bunches out of laser-cooled Rb atoms, using either near-threshold photoionization or field-ionization of Rydberg states. The transverse rms momentum of the bunches is calculated from measurements where the spot sizes of the bunch have been recorded on an MCP detector as a function of current through a magnetic solenoid lens. Varying the solenoid current effectively changes the focal length of the lens, so the bunch sizes on the detector are measured in a so-called 'waist scan'. From a waist scan, a single temperature is obtained by fitting the waist scan for both directions with a GPT simulation that calculates the electron trajectories and includes all important components of the setup.

5.1 Photoionization Experiments

The main set of experiments has been done in a DC electric field that accelerates the electrons after they have been photoionized by a pulsed 480 nm laser. The temperature of these bunches have been determined as a function of excess energy, which is the energy that is available as kinetic energy for the electrons after ionization. Excess energy is dependent on the wavelength of the laser and the Stark shift of the ionization level induced by the electric field strength.

The transverse electron temperature as a function of excess energy shows a non-linear behaviour and is uniform for all measured field strengths. The temperature could be tuned between $T = 10 - 500$ K in the measurements by varying the excess energy. The data overlaps well with earlier measurements from Taban [4]. Three models are used for comparison with the data. The linear model assumes an equal initial momentum distribution in all directions of electrons in the bunch. However, it does not agree with the measurements. It fails to explain the non-linear behaviour and overestimates the transverse temperature for the excess energy range that has

been investigated. It means that in the experiments a part smaller than 1/3 of the total excess energy is put into each of the transverse x and y directions.

A dynamic model follows from calculating the electron trajectories in a potential that consists of a Coulomb term related to the ion core and a linear Stark term related to the applied electric field. For an electron bunch, the transverse momentum distribution then follows at a distance far away from the ion core. These calculations have been done classically [26] and quantum mechanically [25]. They do not completely agree with the data or each other. However, they both predict a similar non-linear temperature behaviour with excess energy as in the data. Moreover, they show just like the data that the transverse temperature is less than can be expected from the linear model.

The classical calculations can be improved by a correct initial distribution of electrons around the ion core. The quantum mechanical calculations can be improved by including the appropriate weighing of the solutions to the Schrödinger equation. Including this together with a more realistic (screened) Coulomb potential might result in a better description of the data.

Temperatures down to $T = 10.7 \pm 0.8$ have been measured, which together with an initial spot size $\sigma_i = 25$ μm and final spot size $\sigma_f = 100$ μm translate into a transverse coherence length of $L_\perp = 36$ nm. This is comparable to the calculated $L_\perp = 38$ nm, which is good enough for single-shot UED of proteins. However, the bunch charge was around $Q = 1 - 10$ fC, the energy $U = 2.5$ keV and the pulse length $\sigma_t = 2.5$ns. This does not compare yet to the ranges of $Q = 100$ fC, $U = 100$ keV and $\sigma_t = 1$ ps needed for actual single-shot UED measurements of protein crystals.

A new series of measurements could be done at higher charge to investigate a lower excess energy regime ($E_{exc} \leq 0.10$ meV) in more detail to see if even lower temperatures are possible. A ps ionization laser can be employed to reach the desired pulse lengths. Higher acceleration voltages can create up to $U = 15$ keV electrons in the current accelerator structure, which might already be enough for study of some crystallic structures. These different conditions will create other difficulties, for example space charge forces that increase the electron bunch size. Some type of bunch compression will then have to used to compensate for this.

5.2 Rydberg State Field-Ionization Experiments

A method for creating cold electron bunches with short temporal lengths is by exciting Rydberg states in Rb atoms, after which electrons are field-ionized by a pulsed electric field. It is not apparent what temperature can be expected from this system and it is also not clear how it depends on

the Rydberg state n. Space charge effects play an important role in these bunches. The measurements show a relation between the bunch momentum and the charge of $\sigma_p \sim \sqrt{Q}$. The measured zero-charge rms bunch sizes can roughly be understood with an overall temperature of about $T = 50$ K. This can be seen as a typical temperature, which shows it is possible to create a low temperature beam also from pulsed Rydberg ionization.

Further investigation of this method could be done with the magnetic solenoid lens, which was not present at the time of the experiments described here. It would give an independent instrument for measuring the temperature of a single Rydberg state, so the temperature behaviour over multiple states could be studied.

5.3 Outlook

The UCP is a new type of source that enables a low transverse temperature for electron bunches. The energy and bunch charge can be further improved in the current setup. Together with short pulse lengths, obtained by a ps ionization laser or pulsed electric field combined with Rydberg states, the UCP setup could be made suitable for single-shot UED experiments. This would enable the study of a whole new range of physical, chemical and biological reactions, both on a very small spatial and temporal scale.

Chapter 5 Conclusion

Bibliography

[1] J. Cao, H. Ihee, and A. Zewail. *Ultrafast Electron Diffraction and Direct Observation of Transient Structures in a Chemical Reaction.* Proc. Natl. Acad. Sci. U. S. A. **96**, 338 (1999).

[2] B. Siwick, J. Dwyer, R. Jordan, and R. Miller. *An Atomic-Level View of Melting Using Femtosecond Electron Diffraction.* Science **302**, 1382 (2003).

[3] V. Lobastov, R. Srinivasan, and A. Zewail. *Four-Dimensional Ultrafast Electron Microscopy.* Proc. Natl. Acad. Sci. U. S. A. **102**, 7069 (2005).

[4] G. Taban. *A Cold Atom Electron Source.* Ph.D. thesis, Eindhoven Uni. of Tech. (2009).

[5] O. J. Luiten, B. J. Claessens, S. B. Van Der Geer, M. P. Reijnders, G. Taban, and E. J. D. Vredenbregt. *Ultracold Electron Sources.* Int. J. Mod. Phys. A **22**, 3882 (2007).

[6] S. B. van der Geer, M. J. de Loos, E. J. D. Vredenbregt, and O. J. Luiten. *Ultracold Electron Source for Single-Shot, Ultrafast Electron Diffraction.* Microsc. Microanal. **15**, 282 (2009).

[7] T. van Oudheusden, E. F. de Jong, S. B. van der Geer, W. P. E. M. O. 't Root, O. J. Luiten, and B. J. Siwick. *Electron Source Concept for Single-Shot Sub-100 fs Electron Diffraction in the 100 keV Range.* J. Appl. Phys. **102**, 093501 (2007).

[8] S. Papadopoulos, K. D. Jurgens, and G. Gros. *Protein Diffusion in Living Skeletal Muscle Fibers: Dependence on Protein Size, Fiber Type, and Contraction.* Biophys. J. **79**, 2084 (2000).

[9] B. Claessens. *Dynamics and Applications of Excited Cold Atoms.* Ph.D. thesis, Eindhoven Uni. of Tech. (2006).

[10] T. Killian, S. Kulin, S. Bergeson, L. Orozco, C. Orzel, and S. Rolston. *Creation of an Ultracold Neutral Plasma.* Phys. Rev. Lett. **83**, 4776 (1999).

[11] R. S. Fletcher, X. L. Zhang, and S. L. Rolston. *Using Three-Body Recombination to Extract Electron Temperatures of Ultracold Plasmas.* Phys. Rev. Lett. **99** (2007).

[12] M. P. Reijnders, P. A. van Kruisbergen, G. Taban, S. B. van der Geer, P. H. A. Mutsaers, E. J. D. Vredenbregt, and O. J. Luiten. *Low-Energy-Spread Ion Bunches from a Trapped Atomic Gas.* Phys. Rev. Lett. **102**, 034802 (2009).

[13] H. Metcalf and P. van der Straten. *Laser Cooling and Trapping.* Springer (1999).

[14] M. Reijnders. Ph.D. thesis, Eindhoven Uni. of Tech. (to be published).

[15] R. Wijtvliet. *Locking a Diode Laser onto an Atomic Rb Line: 2 Spectroscopic Techniques.* Eindhoven Uni. of Tech. (2005).

[16] B. Fleskens. *Ultracold Electron Bunches.* Master's thesis, Eindhoven Uni. of Tech. (2008).

[17] G. Taban. *Design and Validation of an Accelerator for an Ultracold Electron Source.* Phys. Rev. ST Accel. Beams **11**, 050102 1 (2008).

[18] M. G. Littman, M. M. Kash, and D. Kleppner. *Field-Ionization Processes in Excited Atoms.* Phys. Rev. Lett. **41**, 103 (1978).

[19] C. van Ditzhuijzen. *Dipole-Dipole Interactions between Cold Rydberg Atoms.* Ph.D. thesis, Uni. of Amsterdam (2009).

[20] E. Hecht. *Optics.* Pearson (2002).

[21] S. Humphries. *Principles of Charged Particle Acceleration.* Institute for Accelerator and Plasma Beam Technology, Uni. of New Mexico, Albuquerque (1999).

[22] J. Jackson. *Classical Electrodynamics.* John Wiley & Sons, Inc. (1999).

[23] J. Botman. *Particle Accelerators.* Eindhoven Uni. of Tech. (2007).

[24] E. Sachteleben. *Model of Cold Electron Beam Dynamics.* Eindhoven Uni. of Tech. (2007).

[25] J. Sanders. *"Transverse" Kinetic Energy of Photoionized Electrons.* Eindhoven Uni. of Tech. (2009).

[26] C. Bordas. *Classical Motion of a Photoelectron Interacting with Its Ionic Core: Slow Photoelectron Imaging.* Phys. Rev. A **58**, 400 (1998).

[27] H. Bethe and E. Salpeter. *Quantum Mechanics of One- and Two-Electron Atoms.* Academic Press (1957).